Palaeogeography, Palaeoclimatology, Palaeoecology 697 (2026) 113830

Contents lists available at ScienceDirect

Palaeogeography, Palaeoclimatology, Palaeoecology

journal homepage: www.elsevier.com/locate/palaeo

The Early Eocene South Indian subtropical gyre in DeepMIP paleoclimate simulations

Théo Le Hir [a,b,*], Pierrick Penven [a], Thierry Huck [a], Maryline Moulin [b], Marina Rabineau [b], Daniel Aslanian [b]

[a] Univ Brest, CNRS, Ifremer, IRD, Laboratoire d'Océanographie Physique et Spatiale (LOPS), IUEM, Technopôle Brest Iroise, rue Dumont d'Urville, Plouzané, 29280, France

[b] Univ Brest, CNRS, Ifremer, UBS, Geo-Ocean, IUEM, Technopôle Brest Iroise, rue Dumont d'Urville, Plouzané, 29280, France

ARTICLE INFO

Editor: M. Elliot

Keywords:
South Indian subtropical gyre
Early Eocene
DeepMIP

ABSTRACT

The South Indian Subtropical Gyre (SISG) is a major ocean current system contributing to the global circulation. Simulations from the Deep-Time Model Intercomparison Project (DeepMIP) for the Eocene SISG reveal substantial changes in oceanic and atmospheric circulation primarily driven by shifts in paleogeography. The results indicate a reconfiguration and weakening of the gyre no longer connected to the Atlantic (collapsed Agulhas leakage) and extending into the Pacific and a southward displacement of the Subtropical Front (STF). Additionally, the simulations show significantly warmer deep waters (by 9 °C), the disappearance of the freshwater nature of Antarctic Intermediate Water, and a reduced meridional temperature gradient; findings that are broadly consistent with available proxy reconstructions. This study serves as a first step in disentangling robust patterns related to the SISG from inter-model differences of varying magnitude, thereby highlighting the role of model dependency and addressing potential biases in General Circulation Models (GCM) simulating the Eocene.

1. Introduction

1.1. The Indian Ocean subtropical gyre, a major element of the global oceanic circulation

Oceanic gyres are essential for regulating global climate, heat and salinity transport, and carbon cycling. They redistribute warm and cold waters, influencing regional climates, storm patterns, and monsoons. Gyres connect wind-driven and overturning circulation, impacting ocean circulation changes and climate variability over time (Wells, 2003; Hasselmann, 1991). They also play a key role in marine ecosystems, affecting nutrient distribution to fish migration (Reid et al., 1978). The Southern Hemisphere ocean hosts a nested system of three interconnected subtropical gyres in the Atlantic, Indian, and Pacific basins, together forming a supergyre (Ridgway and Dunn, 2007; Tilburg et al., 2001). Located in the southern part of the Indian Ocean, the South Indian Subtropical Gyre (SISG) is an integral component of this larger system (Fig. 1). Circulating counterclockwise, it is bounded by the South Equatorial Current (SEC) to the north (Tomczak and Godfrey, 1994), which moves along the equator towards the east coast of Africa. Once reaching the African coast, the SEC is split by Madagascar into two western boundary currents: the North Madagascar Current (NMC) flowing north and the East Madagascar Current (EMC), which flows south along the eastern coast of Madagascar (Chapman et al., 2003). After passing the northern tip of Madagascar, the NMC flows to the west and splits when reaching the African continent. Its southern branch feeds the Mozambique Channel, dominated by large eddies (Halo et al., 2014). South of the Mozambique Current, the flow merges with the EMC to form the Agulhas Current (AC), the largest western boundary current of the southern hemisphere (Lutjeharms, 2006), transporting 84 Sv (Beal et al., 2015). At the southwestern edge of the Agulhas Bank, the main part of the AC retroflects to flow eastward, giving rise to the Agulhas Return Current (ARC) (Lutjeharms and Ansorge, 2001), while its associated leakage feeds the South Atlantic Ocean. Approximately 15 Sv of warm and salty water from the AC flows into the South Atlantic through Agulhas rings (Richardson, 2007), and this may influence the Atlantic Meridional Overturning Circulation (AMOC) (Beal et al., 2011). The ARC largely recirculates within the subtropical gyre, while the remainder becomes the South Indian Ocean Current (SIOC) beyond 70° E (Lutjeharms and Ansorge, 2001). With the Antarctic Circumpolar Current (ACC), ARC and the SIOC delimit the Subtropical Front

* Corresponding author at: Univ Brest, CNRS, Ifremer, IRD, Laboratoire d'Océanographie Physique et Spatiale (LOPS), IUEM, Technopôle Brest Iroise, rue Dumont d'Urville, Plouzané, 29280, France.

E-mail address: theo.lehir@univ-brest.fr (T. Le Hir).

https://doi.org/10.1016/j.palaeo.2026.113830
Received 25 September 2025; Received in revised form 13 April 2026; Accepted 22 April 2026
Available online 26 May 2026

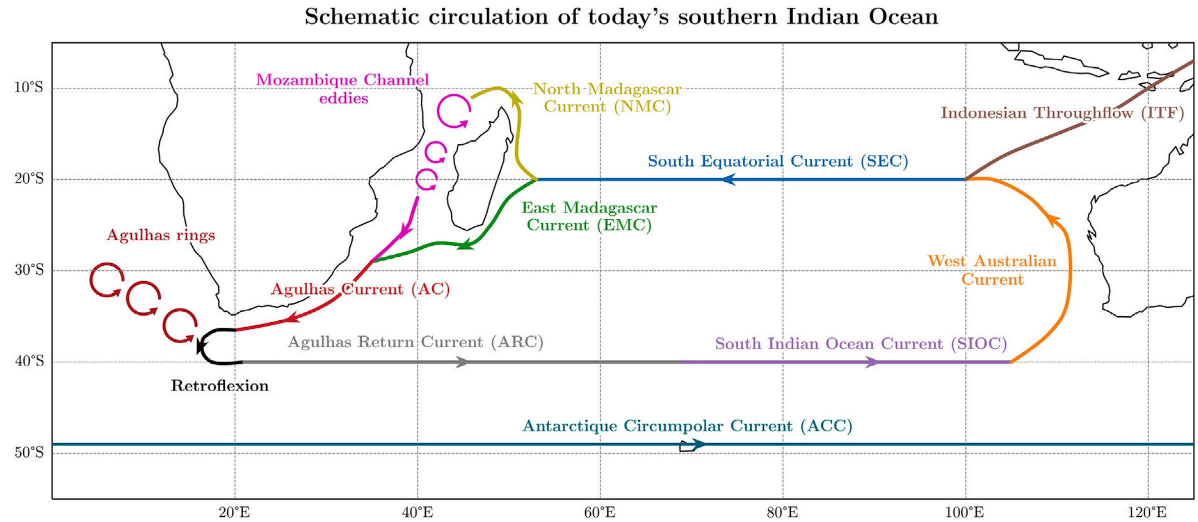

Fig. 1. Schematic circulation of the southern Indian Ocean. The main currents of the SISG are represented.

(STF) separating warm, salty Subtropical Water from colder, fresher Subantarctic Water (Stramma, 1992). A part of the SIOC feeds the West Australian Current, which connects the SIOC to the SEC by flowing northward along the west coast of Australia. This defines the SISG's eastern boundary. The Indonesian Throughflow (ITF) primarily controls the connection between the Indian and Pacific Oceans. The ITF allows warm, low-salinity waters from the western Pacific to enter the Indian Ocean, influencing the dynamics and strength of the gyre (Lambert et al., 2016).

1.2. During the Eocene, the geography, climate and ocean were different

At global scale, Early Eocene (56-50Ma) geography, climate and oceans were markedly different from today. With the Drake Passage and the Tasman Gateway closed (or narrow and shallow compared to today) at the time, strong subpolar gyres were maintained in the Weddell and Ross Seas according to models and neodymium isotopes (Zhang et al., 2020; Huber et al., 2004; Cramwinckel et al., 2020). Similar to the present-day North Atlantic, these subpolar gyres transported saline waters from lower to higher latitudes, sustaining a strong meridional overturning circulation (~40 Sv at 60° S) and enabling significant heat transport in the Southern Hemisphere (Zhang et al., 2020). This mechanism contributed to the weak north–south temperature gradients and the maintenance of temperatures too high for ice sheet formation in Antarctica (Eichenseer and Jones, 2024). Surface temperatures in tropical regions during the Eocene reached 30 to 35 °C, while polar regions experienced a temperate to subtropical climate with temperatures ranging from 10 to 15 °C (Stokke et al., 2020; Sluijs et al., 2020). This extreme warmth is partly attributed to elevated atmospheric CO_2 concentrations, estimated to be three to six times preindustrial levels (Royer et al., 2023). The interannual proxy study by Ivany et al. (2011) using fossil bivalves and sedimentary records from the Eocene indicates quasi-periodic variations in sea surface temperature (SST), precipitation, and sea-level pressure in the equatorial Pacific, consistent with modern ENSO dynamics. Evidence in palynological assemblages suggests that the East Asian Monsoon began to emerge during the Early Eocene, driven by changes in temperature and precipitation patterns (Su et al., 2022). The absence of ice sheets resulted in sea levels up to a maximum of approximately 70 m higher than present (Miller et al., 2024), submerging extensive coastal areas and promoting the formation of epicontinental seas (Lunt et al., 2012). The hydrological cycle was intensified, creating warm and humid conditions even in mid-latitudes (Cramwinckel et al., 2023). Unlike today, where deep water formation occurs in the North Atlantic, during the Eocene, deep waters were primarily formed in the North Pacific as indicated by neodymium isotopes (McKinley et al., 2019), but confirmed only by one over 8 models in numerical studies (Zhang et al., 2022) and in the Southern Hemisphere in agreement with both models and neodymium isotopes (Zhang et al., 2022; Huck et al., 2017).

1.3. Investigating the early Eocene SISG using models in an Early Eocene configuration

These elements suggest that the SISG must have been significantly different from its present-day configuration. Recent progress in paleoclimate modeling, as demonstrated by studies using advanced Earth system models, has enabled increasingly accurate simulations of key aspects of past climate states—including global temperature distributions, precipitation regimes, and large-scale ocean circulation patterns (Lunt et al., 2020; Huber and Caballero, 2011; Zhang et al., 2022). However, these models generally operate at relatively low spatial resolution, which limits their ability to resolve mesoscale features such as oceanic eddies and narrow boundary currents. As a result, it remains uncertain whether they can accurately capture the structure and dynamics of systems like the SISG, particularly in regions where key circulation features depend on mesoscale processes—for example, the eddy-dominated flow through the Mozambique Channel. This limitation poses challenges for assessing the realism of gyre representation in paleoclimate simulations and calls for cautious interpretation of their outputs. This is the focus of our investigation in this study: How was the SISG system during Early Eocene? Can paleoclimate simulations provide insights? What are the robust findings? Are they in agreement with proxy studies? Do models agree with each other on these aspects?

To address these questions, we use multiple simulations carried out within the framework of the Deep-Time Model Intercomparison Project (DeepMIP), which provides a coordinated set of global coupled climate models at pre-industrial and early Eocene periods. These simulations offer a valuable opportunity to investigate the structure of the SISG under markedly different paleogeographic and climatic conditions. We focus on key features of the SISG, analyzing its structure and intensity across the different model outputs. By comparing Eocene simulations with pre-industrial control runs and current reanalysis (modern numerical model that assimilates historical observations), we identify robust patterns and assess inter-model differences. This approach allows us to disentangle the respective contributions of model biases, paleogeography, and atmospheric CO_2 concentrations. We also examine how these simulations align with the available proxy records from the literature. Proxy reconstructions provide indirect constraints on past ocean states and are subject to uncertainties related to calibration and statistical uncertainty in proxy-environment relationships (McClelland et al., 2021). Moreover, proxy records are spatially discrete and may be representative only of local or regional processes, which complicates their extrapolation to basin-scale circulation features resolved by climate models. Additionally, preservation and post-depositional alteration (diagenesis) of proxy carriers can modify original geochemical signals and introduce further uncertainty (Edgar et al., 2015). These uncertainties, combined with potential issues of spatial representativeness and age control in sedimentary archives, mean that many proxy records integrate climate signals over time windows that do not match the model averaging strategy. In all models, the SISG exhibits a markedly different configuration compared to today: the gyre is weaker, extends into the Pacific, with different water masses composition and a collapsed Agulhas leakage. These results highlight the dominant role of paleogeography in shaping oceanic circulation during the Early Eocene. They also provide a foundation for identifying systematic biases in paleoclimate models and for refining future paleoceanographic reconstructions of the Indian Ocean.

2. Models

DeepMIP is a working group within the PMIP4 Paleoclimate Modeling Intercomparison Project, itself part of the sixth phase of the Coupled Model Intercomparison Project, CMIP6 (Eyring et al., 2016). DeepMIP aims to enhance our understanding of "Deep Time" climates through international collaboration. This initiative focuses on geological periods with atmospheric CO_2 concentrations comparable to those projected for the late 22nd century—levels that have no recent equivalent in modern climate archives. Indeed, while current climate models are tested against modern-era observations, they must also be validated using past periods characterized by similarly high CO_2 concentrations. DeepMIP is an excellent opportunity to compare the SISG in various Early Eocene simulations. However, paleoclimate modeling is not without bias. One of the primary limitations is the resolution of the models. The thousands of years of simulations required to reach equilibrium in coupled GCMs for paleoclimate simulations necessitate the use of low-resolution grids (>1° for ocean models) due to computational cost constraints. Nevertheless, fine-scale structures (10–100 km) play a crucial role in ocean circulation, particularly in terms of transport processes, fronts, and mixing layers (Hirschi et al., 2003; Li et al., 2024). This is especially true for the representation of western boundary currents, such as the AC (Schwarzkopf et al., 2019; Holton et al., 2017). For instance, the Agulhas leakage, which connects the Indian Ocean to the Atlantic, occurs through Agulhas rings: eddies that require at least mesoscale resolution to be represented in models (Schubert et al., 2019). The initial conditions and forcings used in simulations (such as greenhouse gas concentration, paleotopography, or ice distribution) often rely on indirect reconstructions, which may contain uncertainties or errors. Convection and vertical mixing are not parameterized in the same way across different models. Paleoclimatic reconstructions (isotopic ratios, foraminifera, etc.) involve uncertainties or may lack data depending on the time periods or regions. The numerical schemes used in models can overly smooth gradients (e.g., temperature, salinity), and so reducing the accuracy of simulations. Interactions between model components (ocean, atmosphere, ice, biogeochemistry) can introduce errors when the couplings are not properly optimized. The nine climate models in the DeepMIP and the Eocene simulations are documented in detail by Lunt et al. (2020). The Eocene paleogeography and bathymetry used in all DeepMIP simulations follow the global reconstructions of Herold et al. (2014), which provide a standardized representation of continental positions, ocean gateways, and seafloor depth for the early Eocene (55 Ma). These reconstructions constitute the common boundary conditions adopted by DeepMIP models (except for NorESM). Zhang et al. (2022) supplement provides additional insights about diapycnal mixing parameterization, bathymetry boundary condition and initial thermohaline conditions. In addition to the various CO_2 experiments, all modeling groups were required to carry out a pre-industrial (PI) simulation for comparison purposes, which was to be as close as possible to the CMIP6 standard PI-Control simulation (Eyring et al., 2016) (see Table 1).

Eocene boundary conditions are significantly different from those of the present day, implying that these simulations initialized with crude ocean thermohaline structures will require several millennia to reach an equilibrium state (Kennedy-Asser et al., 2020). Over the last 1000 years of simulation, deep ocean temperature trends are less than 0.5 °C.

The first step of this study will be to determine robust patterns in the low-resolution modeling of GCMs by comparing DeepMIP PI outputs to state-of-the-art reanalyses and climatologies, such as GLORYS (Lellouche et al., 2018) for ocean circulation, the World Ocean Atlas 2023 (WOA) for water mass properties at 1/4° resolution (Reagan et al., 2024) and the European Centre for Medium-Range Weather Forecasts (ECMWF) Reanalysis v5 (ERA5) for atmospheric conditions (Hersbach et al., 2020).

3. Methods

In this study, we analyzed the SISG of seven DeepMIP GCMs. These models include CESM1.2 (hereafter CESM), COSMOS-landveg-r2413 (hereafter COSMOS), GFDL-CM2.1 (hereafter GFDL), IPSL-CM5A2 (hereafter IPSL), MIROC4m (hereafter MIROC), HadCM3B and HadCM3BL. For each of these models, we will compare three configurations: the pre-industrial configuration (hereafter PI) with a CO_2 level of 280 ppm, an early Eocene configuration with the same CO_2 level as PI (hereafter paleo x1 CO_2), and an early Eocene configuration with three times the CO_2 level of paleo x1 CO_2, i.e., 840 ppm (hereafter paleo x3 CO_2). We do not include INMCM or NorESM, as neither has a paleo x3 CO_2 configuration. Additionally, for wind stress analysis, we exclude COSMOS as it does not provide wind stress as an output. The outputs provided by DeepMIP consist of monthly climatologies (averaged over the last 100 years of each simulation) and monthly time series for the last 100 years. The variables are described and made available as open access (Steinig et al., 2024). Given the differences in grid configurations, we pre-processed the model outputs to a higher resolution to preserve maximum information. Temperature and salinity vertical sections are re-interpolated linearly on grids with a 0.5° latitudinal resolution and 5 m vertical resolution. We analyzed the SISG within a domain covering the southern part of the Indian Ocean (70° S–0° S, 0° E–150° E) for the following variables: wind stress curl, barotropic streamfunction, STF, water masses, and Rossby deformation radius, as detailed in the next subsections.

3.1. Mean wind stress curl

Wind Stress Curl is the forcing factor of the Sverdrup balance (Sverdrup, 1947):

$$\beta \frac{\partial \psi}{\partial x} = \frac{\nabla \times \boldsymbol{\tau}}{\rho}$$

where $\beta = \frac{\partial f}{\partial y}$ ($s^{-1}\,m^{-1}$) is the meridional gradient of the Coriolis parameter f (s^{-1}), ψ ($m^3\,s^{-1}$, hereafter expressed in Sverdrups with $1\,Sv = 10^6\,m^3\,s^{-1}$) is the barotropic streamfunction (with $V = \frac{\partial \psi}{\partial x}$ the vertically integrated meridional transport, in $m^2\,s^{-1}$), ρ is the seawater density ($kg\,m^{-3}$), and $\nabla \times \boldsymbol{\tau} = \frac{\partial \tau_y}{\partial x} - \frac{\partial \tau_x}{\partial y}$ is the wind stress curl ($N\,m^{-3}$), the direct driver of oceanic gyres. Position and intensity of oceanic gyres can vary on geological timescales. Zhang et al. (2025) demonstrated that this is the case for the North Pacific Gyre, which shifted northward at the onset of the Eocene, primarily driven by wind-driven transport. In our case, the computation of the curl requires evaluating τ_x and τ_y on the sides of each grid cell. This implies that land masks are slightly modified, which can impact the calculation more significantly at lower resolutions (for example, it leads to a closed Mozambique Channel for HadCM3BL). The zonally-averaged wind stress curl is calculated over the region spanning 50° E to 100° E, away from continental masses.

Table 1
Summary of paleoclimate models participating in DeepMIP: laboratory affiliation, experiments performed, ocean grid resolution and type, and simulation length.

Model	Laboratory	CO_2	(lat × lon), z levels	Ocean Grid	Run length (yr)
CESM1.2-CAM5	NCAR (USA)	×1, ×3, ×6, ×9	(1° × 1°), 60	Greenland grid (polar shifted)	2000–2600
COSMOS-landveg-r2413	MPI-M (Germany)	×1, ×3, ×4	(3° × 1.8°), 40	Bipolar curvilinear	9500
GFDL-CM2.1	NOAA-GFDL (USA)	×1, ×2, ×3, ×4, ×6	(1° × 1.5°), 50	Tripolar	6000
HadCM3B-M2.1aN	Met Office Hadley Centre (UK)	×1, ×2, ×3	(1.25° × 1.25°), 19	Cartesian	7400
HadCM3BL-M2.1aN	Met Office Hadley Centre (UK)	×1, ×2, ×3	(3° × 2.5°), 20	Cartesian	7500
INMCM-CM4-8	INM (Russia)	×6	(1° × 0.5°), 40	Generalized spherical (C-grid)	1150
IPSLCM5A2	IPSL (France)	×1.5, ×3	(2° × 2°), 31	Tripolar	4000
MIROC4m	CCSR/NIES/ FRCGC (Japan)	×1, ×2, ×3	(1° × 1°), 44	Regular grid with tropics refinement	5000
NorESM1-F	Norwegian Climate Center (Norway)	×2, ×4	(1° × 1°), 46	Tripolar	2100

3.2. Mean barotropic streamfunction, Agulhas leakage, gyre recirculation and ACC transports

The barotropic streamfunction ψ represents the depth-integrated mean horizontal flow and is a key diagnostic for identifying the structure and strength of large-scale ocean gyres. It is derived from the curl of the barotropic velocity field, ensuring mass conservation and representing the circulation around islands and continental boundaries. In this study, the streamfunction is computed by following a Helmholtz decomposition by solving a Poisson equation using a method that incorporates both a particular solution for the domain and homogeneous solutions for individual islands. The final solution is constructed to ensure that the circulation around each island matches that imposed by the barotropic transport field. This method, based on the framework of Colin de Verdière and Ollitrault (2016) and solved via successive over-relaxation (Yang and Matthias, 2007), is detailed in the first section of the appendix document. Because the DeepMIP simulations provide low-frequency (climatological) output, the Agulhas leakage is diagnosed here by identifying streamlines of ψ that connect the Indian and Atlantic Oceans under specific geometric and directional criteria rather than using Lagrangian methods (Richardson, 2007). These include crossing key transects (e.g., the Good Hope Line and 40° E) and flowing from east to west north of the STF. This method is detailed in the second section of the appendix. By applying this method to the annually-averaged GLORYS horizontal transport, we obtain 13.1 Sv, which is close to the value derived from the Lagrangian method applied to observations (Richardson, 2007) and from eddy-resolving simulations (Schmidt et al., 2021). The subtropical gyre circulation is defined as the difference between the maximum of ψ in the center of the recirculating subgyre and the Agulhas leakage. This gives 69.8 Sv for GLORYS which is close to the 66 Sv from Dijkstra and De Ruijter (2001). For the ACC, we take the transport value closest to Antarctica (this value should be at first order independent of longitude). This gives a value of 151.2 Sv for GLORYS which is slightly lower than the recent measure at the Drake passage 173.3 ± 10.7 Sv (Donohue et al., 2016).

3.3. STF position and water masses

To study the STF position, which marks the southern boundary of the gyre and separates warm subtropical waters from cold subpolar waters, we define temperature and salinity sections across the Mozambique Channel. Additionally, the STF plays a crucial role in the connection between the SISG and the Atlantic Ocean (Dencausse et al., 2011) which makes it interesting for us to study. Salinity sections also provide insight in the representation of water masses. For the temperature sections, we computed the SST difference along the section between the two latitudes 60° S and 15° S at 10 m depth (noted Δ_ySST). In paleoclimate simulations, the characteristic salinity and temperature values of water masses can differ significantly from those of the present day. Therefore, the method for identifying the STF described by Belkin et al. (1998) cannot be applied. Instead, the position of the STF is determined as the latitude corresponding to the maximum meridional temperature gradient along the section at 10 m depth. Vertical profiles of temperature, salinity, and density averaged over the SISG region provide insights into water mass characteristics. We analyze water mass composition using Θ–S diagrams computed over 20° S–40° S and 50° E–100° E, interpolated onto a common z-grid to allow envelope representation. Stratification defined by the square of the buoyancy frequency N^2 (s^{-2}), is examined over the upper 750 m, where most variations occur. This approach helps trace the origin of water masses within the gyre and assess how they respond to different experimental conditions.

3.4. Rossby deformation radius (R_0)

Finally, we examine the typical size of the oceanic mesoscale eddies that would develop through the instability of large scale currents if the model resolution were sufficient. As conveyors of heat, salt, momentum and marine properties, mesoscale eddies are dominating the present oceanic circulation (Chelton et al., 2007; Ferrari and Wunsch, 2009). As the mesoscale eddy length scales have been observed to align with the Rossby deformation radius (R_0 hereafter expressed in km) (Stammer, 1997), this parameter should give first insights of the mesoscale eddy properties of the past (even in non eddy resolving simulations). This length scale depends on the ocean depth and stratification, and the local rotation of the Earth (the Coriolis parameter). For this purpose, we compute the Rossby deformation radius, which defines the length scale of baroclinic instability, directly influencing eddy size and baroclinic wave propagation (Chelton et al., 1998). Rossby deformation radius is directly affected by the large changes in bathymetry and stratification between paleo and pre-industrial simulations. Rossby deformation radius is obtained by solving the eigenvalue problem for the vertical structure of perturbations horizontal velocities (λ_n^2, with the associated Rossby deformation radius $R_n = \lambda_n^{-1}$ Chelton et al., 1998):

$$\partial_z \left(\frac{f^2}{N^2} \partial_z F \right) + \lambda_n^2 F = 0$$

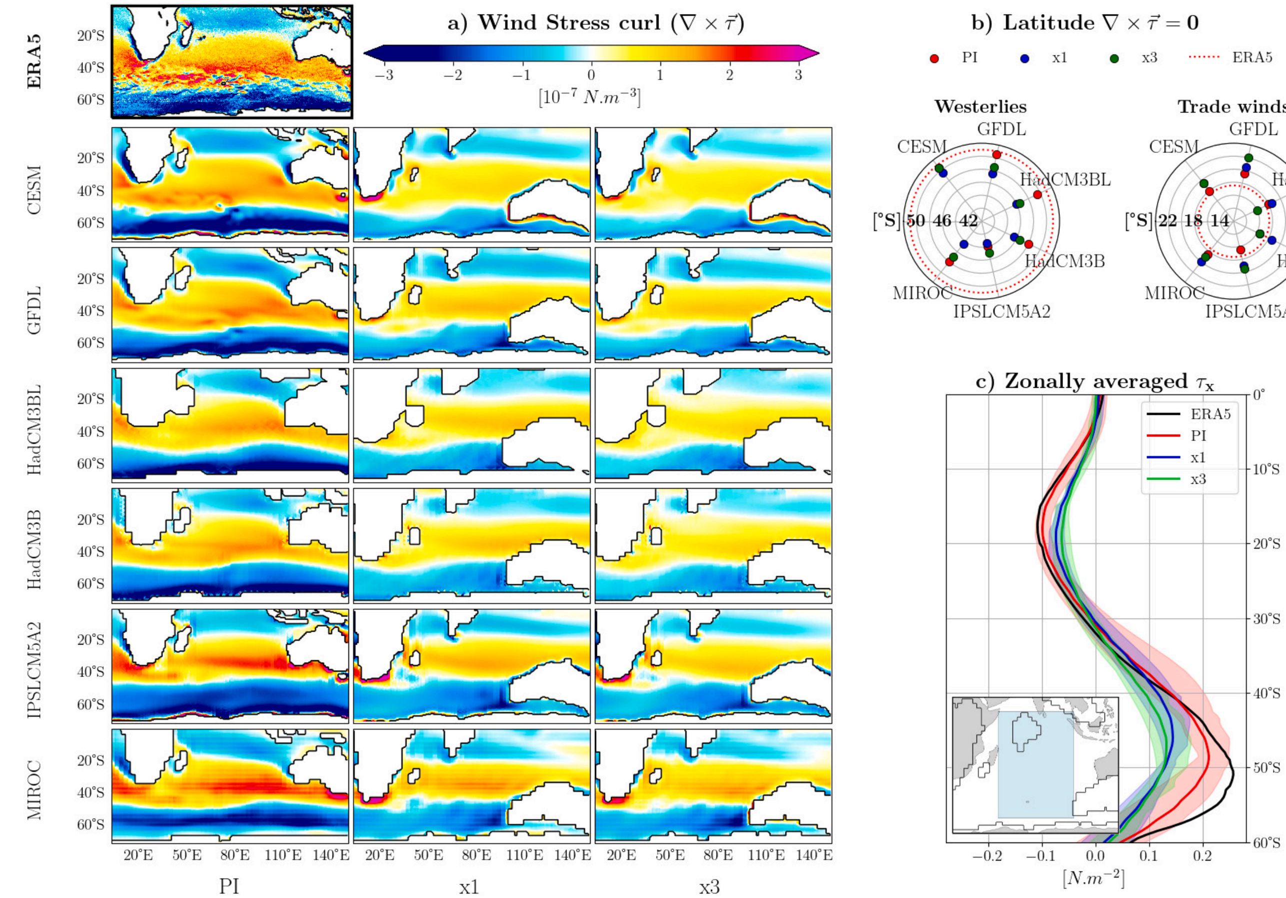

Fig. 2. (a) Annual-mean wind stress curl [10^{-7} N m^{-3}] for the PI, paleo x1 CO_2, and paleo x3 CO_2 configurations of six DeepMIP model outputs, as well as the 2000–2009 average from the ERA5 atmospheric reanalysis. Blue/red values indicate anticyclonic/cyclonic (clockwise/anticlockwise in the Southern Hemisphere) wind forcing. (b) Radial scatter plot, showing the deviation of the maximum westerlies and trade winds in degrees, defined as the mean latitude of the zero wind stress curl between 50° E and 100° E (blue shaded area on the map). (c) Annual-mean zonal wind stress (τ_x, positive eastward), zonally-averaged over 50° E–100° E, for the ERA5 reference (black), averaged over the PI configurations (red), paleo x1 CO_2 configurations (blue), and paleo x3 CO_2 configurations (green). The associated shaded areas indicate the inter-model spread. (For interpretation of the references to color in this figure legend, the reader is referred to the web version of this article.)

with surface and bottom boundary conditions $\partial_z F = 0$ at $z = 0$ and $z = -H$. In this formula, the Brunt–Vaisala frequency N (defined as $N^2 = -\frac{g}{\rho_0}\partial_z \rho$) is computed using the potential density ρ (kg m^{-3}) calculated with an empirical relationship (McDougall et al., 2009) as a function of temperature and salinity, which are interpolated level by level onto a common 3D z-grid (1000 regularly spaced vertical levels).

4. Results

4.1. Wind stress curl: A shifted and weakened wind circulation system

By controlling Sverdrup transport, wind stress curl directly drives the large-scale gyres. It plays a key role in their development and maintenance by inducing horizontal pressure gradients that sustain geostrophic flows (Sverdrup, 1947). Positive wind stress curl (Fig. 2a, red orange and yellow areas) are associated with equatorward meridional velocities in the interior ocean and poleward return current along the western boundary, driving an anticyclonic circulation in the southern hemisphere, typical of subtropical gyres. At present day, trade winds (with a maximum around 17° S in ERA5) are driven by the Hadley cell which drives tropical circulation with rising air at the equator and sinking at the subtropics, while westerly winds (peaking around 51° S in ERA5) are driven by the Ferrel cell, the mid-latitude overturning air circulation that moves in the opposite direction of the Hadley cell (Fairbridge, 2005). Their maxima are identified using the zonally-averaged zero wind stress curl. With varying wind stress intensity and westerly wind positions (Figs. 2b, c), the PI outputs produce a tripolar wind circulation system. Theoretical frameworks link the poleward boundary of the subtropical gyres to the latitude where the wind stress curl is zero (De Ruijter, 1982). The position and intensity of oceanic gyres vary on geological timescales.

The most robust results across the model runs from this figure are the weakening of the entire wind circulation system and the northward shift of the westerlies in the Eocene simulations (Fig. 2a, columns X1 and X3). Models unanimously show a decrease in the zonal wind stress, with an average reduction of ~50% (Fig. 2c). This is consistent with Zhang et al. (2022), who found a lower wind stress in the x3 configuration compared to the PI configuration for the IPSL model in the Southern Hemisphere. This is also the case for other models, even in the paleo x1 CO_2 configurations. This indicates that CO_2 is not the only driving force behind the weakening of wind stress. This phenomenon is explained by the past continental configuration, which enhances meridional heat transport (Zhang et al., 2022) and tends to reduce the meridional temperature gradient (a weaker meridional temperature gradient is observed and discussed later), which plays a key role in atmospheric circulation (Chelton et al., 2001). A decrease in wind stress curl is also observed in the Pacific part of the supergyre (Zhang et al., 2025), and this change is associated with Australia, which forms an orographic obstacle in the Eocene simulations. The Eocene x3 CO_2 simulations show a northward shift of the westerlies in all models (3.6°

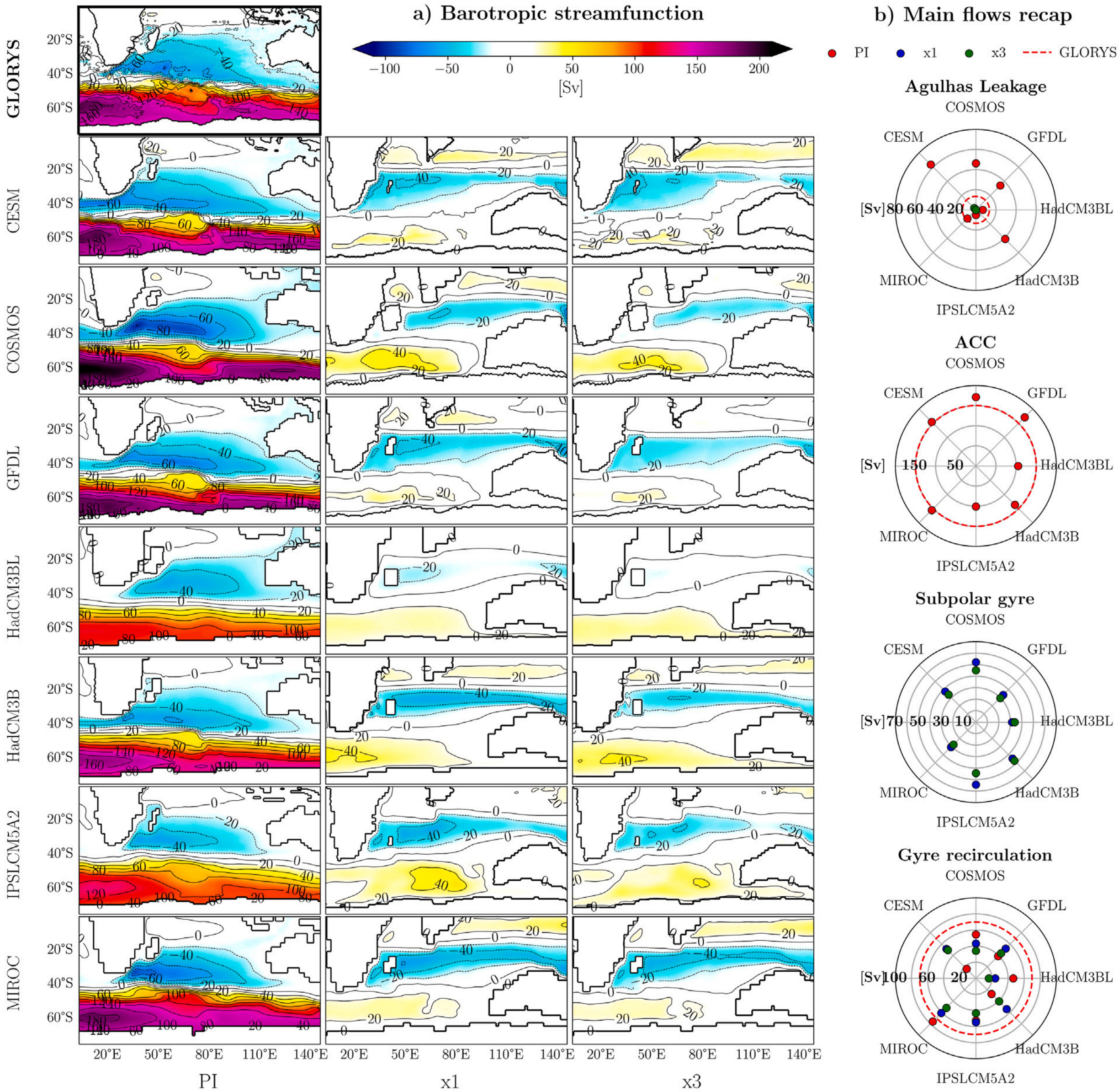

Fig. 3. (a) Mean barotropic streamfunction [Sv] for the PI, paleo ×1 CO_2, and paleo ×3 CO_2 configurations from seven DeepMIP model outputs, and for the GLORYS reanalysis averaged over 2000–2009. (b) Radial scatter plots of the main flows (Agulhas leakage, ACC, Subpolar Gyre, and Retroflection) for GLORYS and each DeepMIP simulation. Note that only PI models are shown in the ACC scatter plot, as the ACC is absent in the paleo x1 CO_2 and paleo x3 CO_2 configurations. Similarly, the PI configuration is not shown in the Subpolar Gyre scatter plot, as this gyre exists only in the paleo x1 CO_2 and paleo x3 CO_2 configurations.

on average compared to ERA5). This shift is even more important in the paleo x1 CO_2 simulation (5.2°) and is attenuated by the increased CO_2. A less robust result is the southward shift of the trade winds (1.4°). However, this shift is more robust (and important) in the paleo x1 CO_2 simulations (2.3°). As a result, we also note that the Eocene simulations show better intermodel agreement compared to the PI simulations.

4.2. Barotropic streamfunction: A reshaped and weaker gyre system

The barotropic streamfunction ψ is primarily driven by the wind stress curl at the center of the gyre but is strongly influenced by other dynamical processes such as bottom pressure torque or inertial and viscous effects in the case of a western boundary current like the AC (Penven et al., 2021). As ψ is defined relative to an arbitrary additive constant (Fig. 3a), we set $\psi = 0$ on the African continent. Positive/negative values mean anticlockwise/clockwise integrated transport relative to Africa. For example, AC (clockwise compared to Africa) leads to negative values. Fig. 3b summarizes the value of the Agulhas Leakage, the ACC, the subpolar gyre and gyre recirculation. When applied to GLORYS reanalysis, the method gives values close to those found in the literature. When applied to the PI simulations, it gives strongly varying results: Agulhas Leakage is ranging from 5.2 Sv for IPSL to 63.6 Sv for CESM. This may be attributed to several factors, such as the position of the STF. ACC transport values range from 101.5 Sv for IPSL to 172.9 Sv for GFDL, we did not prospect the origin of these variabilities, whose transport is controlled by numerous factors such as the westerly wind stress, density gradients, eddy activity, and bathymetry (Lamy et al., 2024). The inter-model spread in subgyre recirculation is also high, ranging from 16.6 Sv for CESM to 76.0 Sv for MIROC. This should be linked to the overestimation of the Agulhas leakage because if we look at the maximum of the SISG (the AC transport), only IPSL and HadCM3BL are significantly lower than GLORYS.

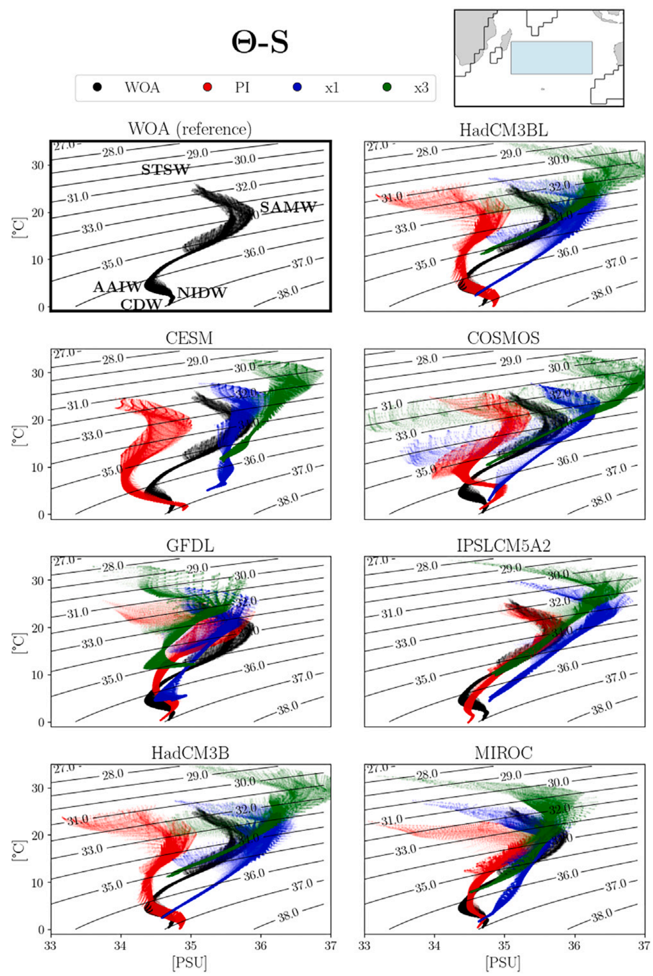

Fig. 4. Θ-S diagrams for the central subtropical gyre (20° S–40° S, 50° E–100° E; blue shaded area on the map) for the reference World Ocean Atlas (shown in black in each subplot) and 7 models under the 3 configurations. Contours indicate potential density anomaly (kg m^{-3}). Main water masses of the area are represented on the top left reference panel: STSW (SubTropical Surface Water), SAMW (South Atlantic Mode Water), AAIW (Antarctic Intermediate Water), NIDW (North Indian Deep Water) and CDW (Circumpolar Deep Water). (For interpretation of the references to color in this figure legend, the reader is referred to the web version of this article.)

Compared to the PI configurations, the Early Eocene simulations show radical changes in the SISG and the Indian Ocean circulation in general. Across all models, SISG is no longer exclusively connected to the South Pacific via the ITF and Tasman Leakage. Instead, part of the flow expands across the entire Pacific (Fig. 3a), passing north of Australia and merging with the South Pacific Subtropical Gyre to form a "supergyre", following the formulation used by Zhang et al. (2025) to describe this connection. A portion of the flow continues to recirculate within the Indian Ocean. This recirculating component can be quantified by subtracting the Pacific outflow from the total retroflection. Here, we do not explicitly represent the Pacific portion of the gyre. This component is illustrated by Zhang et al. (2025). In all simulations, mid-latitudes transport between the Indian and Pacific Oceans is enhanced under this new configuration. A subtropical cyclonic gyre takes place east of India in all Eocene simulations, the ACC no longer exists, and a cyclonic subpolar gyre is developing in the Austral region with a flow ranging from 31.5 Sv for HadCM3BL to 53.0 Sv for IPSL. This gyre is carrying water from mid to high latitudes and thus, contributes to keep a weak meridional temperature gradient. This should maintain a much weaker SISG (especially considering the absence of leakage). The AC (Agulhas leakage + Gyre recirculation) is ranging from 15.9 Sv for HadCM3BL to 56.9 Sv for MIROC in the x3 simulation (CO_2 also contributes to this weaker circulation) against an average of 74.4 Sv for the PI simulations and 73.2 Sv for GLORYS. In all Eocene simulations, the boundary between the subtropical and the subpolar gyre (shown by the $\psi = 0$ contour in Fig. 3a) connects to the southern tip of Africa, indicating the absence of Agulhas leakage. This is largely due to the southward shift of the position of Africa now intersecting the STF. Indeed, Africa is much further south (~10°) than the average STF poleward shift (3.7° in average in the paleo x1 CO_2 simulations).

4.3. Water masses temperature and salinity in the DeepMIP simulations

To understand the thermohaline changes in the SISG region, we analyze the water masses represented in the different DeepMIP simulations. These are traditionally explored using Θ-S diagrams, where potential temperature Θ replaces depth on the vertical axis and salinity S is on horizontal axis. Fig. 4 shows these diagrams for the central subtropical gyre (20° S–40° S and 50° E–100° E) for each model and configuration (PI, paleo x1 CO_2, and paleo x3 CO_2). In addition to Θ-S diagrams, vertical profiles of temperature, salinity, and density are shown in Figs. 5c, 6b and 6c for the same region. These reveal the vertical structure and variability across models. The meridional SST gradients are summarized in the radial scatter plot in Fig. 5b. Figs. 5a and 6a present meridional sections of temperature and salinity along the Mozambique Channel (42° E for the present configurations and 37° E for the paleo configurations).

We identify in Fig. 6 the different water masses of the western part of the Indian Ocean in the WOA salinity section, which are not the same as the ones identified in the middle of the gyre. The Subtropical Surface Water (STSW) occupies the uppermost layer of the water column, typically found above 200 m depth. It is characterized by relatively high salinity due to evaporation higher than precipitation in subtropical regions. It is bordered at south by the STF. Red Sea Water (RSW) is present at intermediate depths, usually between 900 and 1200 m. This water mass originates from the Red Sea and is known for its high salinity and temperature. AAIW is found at depths around 1000 m. It is characterized by lower salinity compared to surrounding water masses, as it originates from the colder, fresher waters around Antarctica. North Atlantic Deep Water (NADW) is found at greater depths, typically between 2200 and 3500 m. This water mass is formed in the North Atlantic and is characterized by relatively high salinity and oxygen content. North Indian Deep Water (NIDW) is generally found in the deep layers of the Indian Ocean and may be present in the northern parts of the Mozambique channel (Sætre and Da Silva, 1984). Harms et al. (2019) identified water masses in the center of the gyre using CTD measurements in our study region and found a structure similar to that given by WOA (Fig. 4). In order of increasing temperature, these include Circumpolar Deep Water (CDW), present at depth and mainly in the southern part of the region, NIDW, AAIW, Subantarctic Mode Water (SAMW) located between isopycnals 1034.5 and 1035.5 kg m^{-3} and STSW.

DeepMIP PI models fail to accurately represent the water masses within the exact salinity range of their counterparts (differences with WOA) in the western part of the basin, they still manage to capture the structures shapes (Fig. 6a). Specifically, the AAIW subducts beneath the STSW. The intermediate waters originating from the northern part of the channel (RSW) is effectively saltier than the AAIW coming from the south. This result is also observed when comparing the models in the center of the gyre. The Θ-S diagrams successfully capture the general shape of the water masses (convex, then concave, then convex when moving from low to high density), except for HadCM3B (convex then concave). IPSL, in particular, closely matches WOA. GFDL and MIROC are also sufficiently close to WOA to represent deep water. Down to 1000 m depth (over 5 °C, Fig. 5d), the salinity and temperature

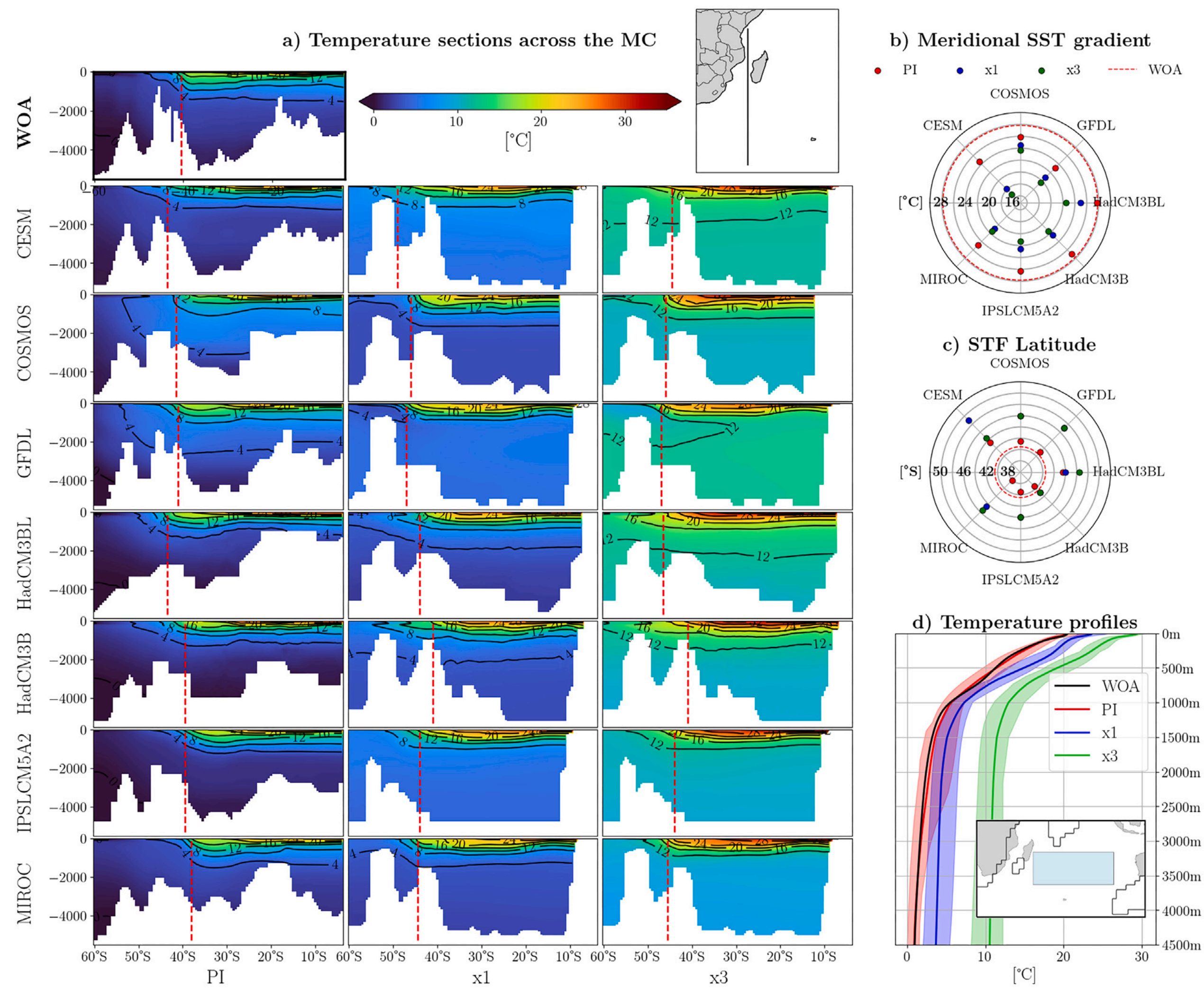

Fig. 5. (a) Temperature meridional section in the middle of the Mozambique Channel (42° E for the present configurations and 37° E for the paleo configurations; see map) for the PI, paleo x1 CO_2, and paleo x3 CO_2 configurations of 7 DeepMIP models and WOA. The vertical red line represents the location of the maximum meridional SST gradient. Blue/red indicate cold/warm water. (b) Radial scatter plot representing maximum SST meridional gradients for each DeepMIP models. (c) Radial scatter plot representing STF latitude for each DeepMIP models. (d) Vertical profiles of temperature averaged over 20° S–40° S and 50° E–100° E (blue shaded area on the map) averaged over the PI configurations (red), paleo x1 CO_2 configurations (blue), and paleo x3 CO_2 configurations (green). The associated shaded areas indicate the inter-model spread. (For interpretation of the references to color in this figure legend, the reader is referred to the web version of this article.)

profiles exhibit a mean bias that is respectively negative and positive compared to WOA. This results in a negative bias in the density profile (on average across all models). This pattern is also observed in the T-S diagrams, where below the isopycnal 1035 kg m^{-3} all models except IPSL are negatively shifted in salinity relative to WOA. Salinity profiles exhibit significant inter-model variability at the surface and subsurface, depending on whether they advect the STSW southward or not. There is a significant inter-model spread in terms of isotherm depth (Fig. 5a). Examining the 4 °C isotherm in the MC section it reveals differences between the models: GFDL and COSMOS 4 °C isotherm is way deeper (~2500 m) than WOA (~1500 m). The north–south temperature gradients at a depth of 10 m are slightly weaker in the DeepMIP simulations compared to WOA, with a difference ranging from 0.1 °C lower for HadCM3BL to 4.7 °C for GFDL (Fig. 5b). This could contribute to explain the weaker westerlies system observed on Fig. 2. The temperature/salinity averaged across the models align well with WOA, with an inter-model spread of less than 1 °C/0.2 PSU, which is reflected in the density profiles.

4.4. Warmer and saltier subtropical gyre with no AAIW during Eocene

Overall, the paleo configurations lead to a warmer and saltier SISG. On average, across all models, the temperature shift is approximately 3 °C throughout the water column for paleo x1 CO_2 and around 9 °C for x3 (Fig. 5c). Regarding salinity, the shift is primarily driven by changes in geography and occurs mainly in shallow waters (<1500 m in the profiles). This could be explained by the SISG being much more extended, stretching eastward and reaching north of Australia up to South America (Zhang et al., 2025). As a result, the SEC propagates over thousands of kilometers at 20° S, allowing it ample time to warm up and accumulate high salinity through evaporation before forming the STSW (as observed in the salinity sections). Deep waters properties are affected by a reorganization of the location of deep water formation towards the Southern Ocean. The closed Drake and Tasman gateways promoted a *salt-advection feedback mechanism*, similar to the present-day overturning circulation of the North Atlantic, which sustained the poleward advection of saline subtropical water to the convective regions of the Southern Ocean (Zhang et al., 2020). This salinity shift at the sea surface and subsurface compensates for the warmer temperature

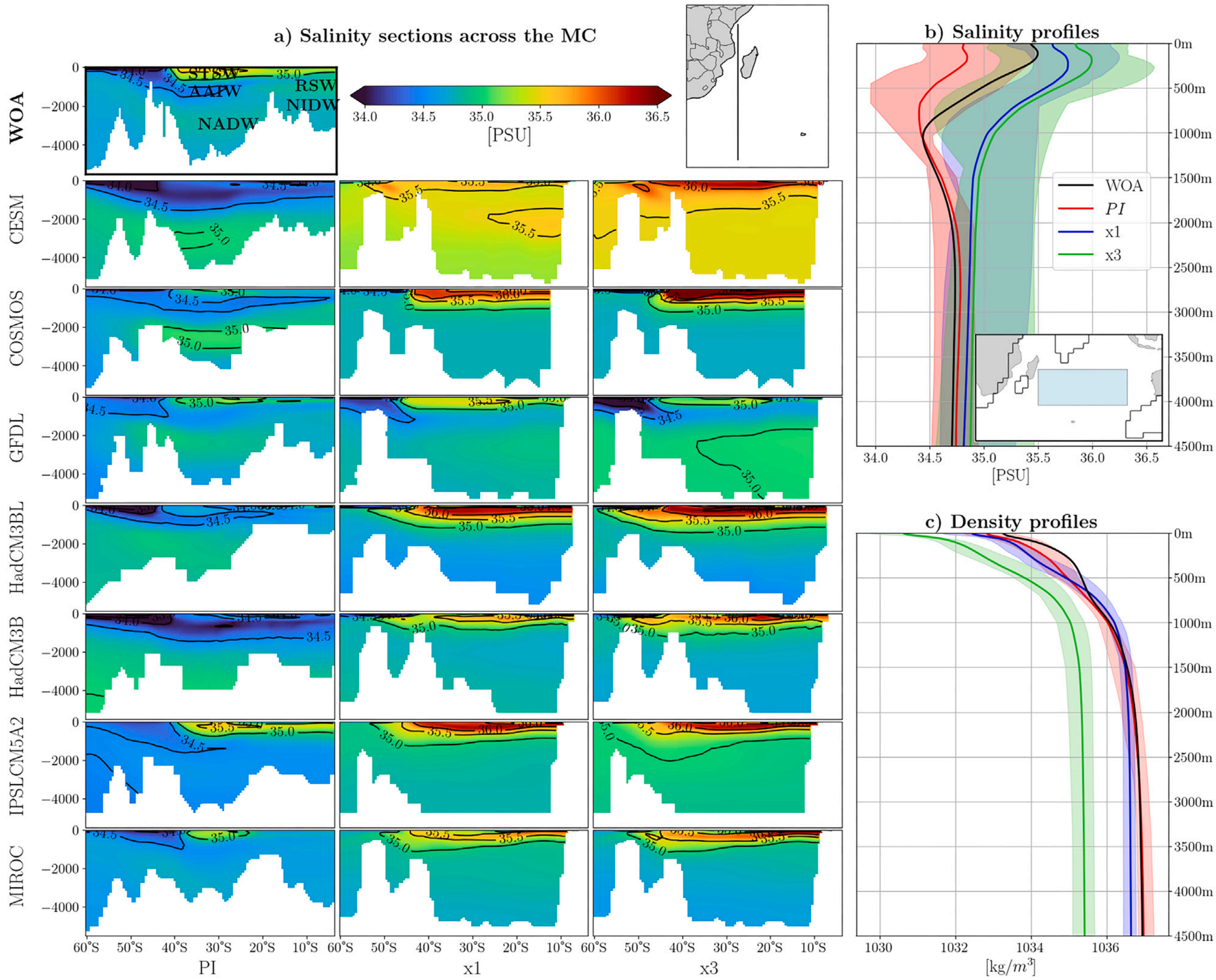

Fig. 6. (a) Meridional salinity sections in the middle of the Mozambique Channel (42° E for the present configurations and 37° E for the paleo configurations; see map) for the three DeepMIP configurations and WOA (top-left). Blue/red indicate fresh/salty water. Water masses are labeled in the WOA section. (b) Salinity and (c) density vertical profiles averaged over 20° S–40° S and 50° E–100° E (blue shaded area on the map) averaged over the PI configurations (red), paleo x1 CO_2 configurations (blue), and paleo x3 CO_2 configurations (green). The associated shaded areas indicate the inter-model spread. (For interpretation of the references to color in this figure legend, the reader is referred to the web version of this article.)

in terms of seawater density down to 2000 m. The influence of these changes on density profiles highlights the α-behavior (temperature influence density more than salinity) of the ocean in these simulations, which is consistent with present-day conditions (Stewart and Haine, 2016). The Θ-S diagrams (Fig. 4) and salinity sections (Fig. 6a) show that the freshwater peak associated with AAIW is only represented by GFDL in the paleo x1 CO_2 and paleo x3 CO_2 configurations. However, while the surface waters are saltier in paleo x1 CO_2 and paleo x3 CO_2 configurations, deep water salinity is not significantly affected by the paleo configuration (except for CESM, Fig. 6a) in contrast with deep water temperature, which reaches extremely high values up to 12.5 °C at 4500 m (Fig. 5c). This results in a linear relationship between temperature and salinity at a density greater than 1034 kg m^{-3} and a change in the Θ-S curve shape from convex–concave–convex to convex-linear (it is less clear for CESM and remaining convex–concave for GFDL). A final key result, previously mentioned and carrying important implications for wind circulation and consequently for precipitation, is the meridional temperature gradient. This gradient, associated with changes in oceanic transport and the transformation of the ACC into a polar gyre, decreases markedly from 11 °C in CESM to 4.1 °C in COSMOS.

4.5. *Poleward shift of the STF*

Tightly associated with the southern boundary of the subtropical gyre, the location of the STF provides a synthetic indicator of the ocean dynamics. We first compare temperature sections (as a function of latitude and depth) across the Mozambique Channel from 60° S to 5° S for each of the seven DeepMIP models in the three configurations (PI, paleo x1 CO_2, and paleo x3 CO_2), and for the WOA (1/4°) realistic reference (Fig. 5a). The STF positions relative to those from WOA are calculated according to the method described in Section 3 and summarized in the radial scatter plot in Fig. 5b. DeepMIP PI simulations place the STF between 37.5° S and 43° S, which is consistent with the 40.5° S position from WOA salinity and temperature sections (Figs. 5a and 6a). Except for IPSL, the other PI-models underestimate surface salinity values north of the front, making it difficult to visualize in these sections (Fig. 6a). In the configurations paleo x1 CO_2, on the temperature sections, the STF shifts southward, ranging from a 1.5° displacement for HadCM3B to 6.5° for MIROC. Except for CESM and HadCM3B, the front's position also appears in the salinity sections, with a significantly more pronounced meridional SSS gradient than in the PI configuration, particularly for IPSL, HadCM3BL, and COSMOS. CO_2 impact on the front position is not robust across all models.

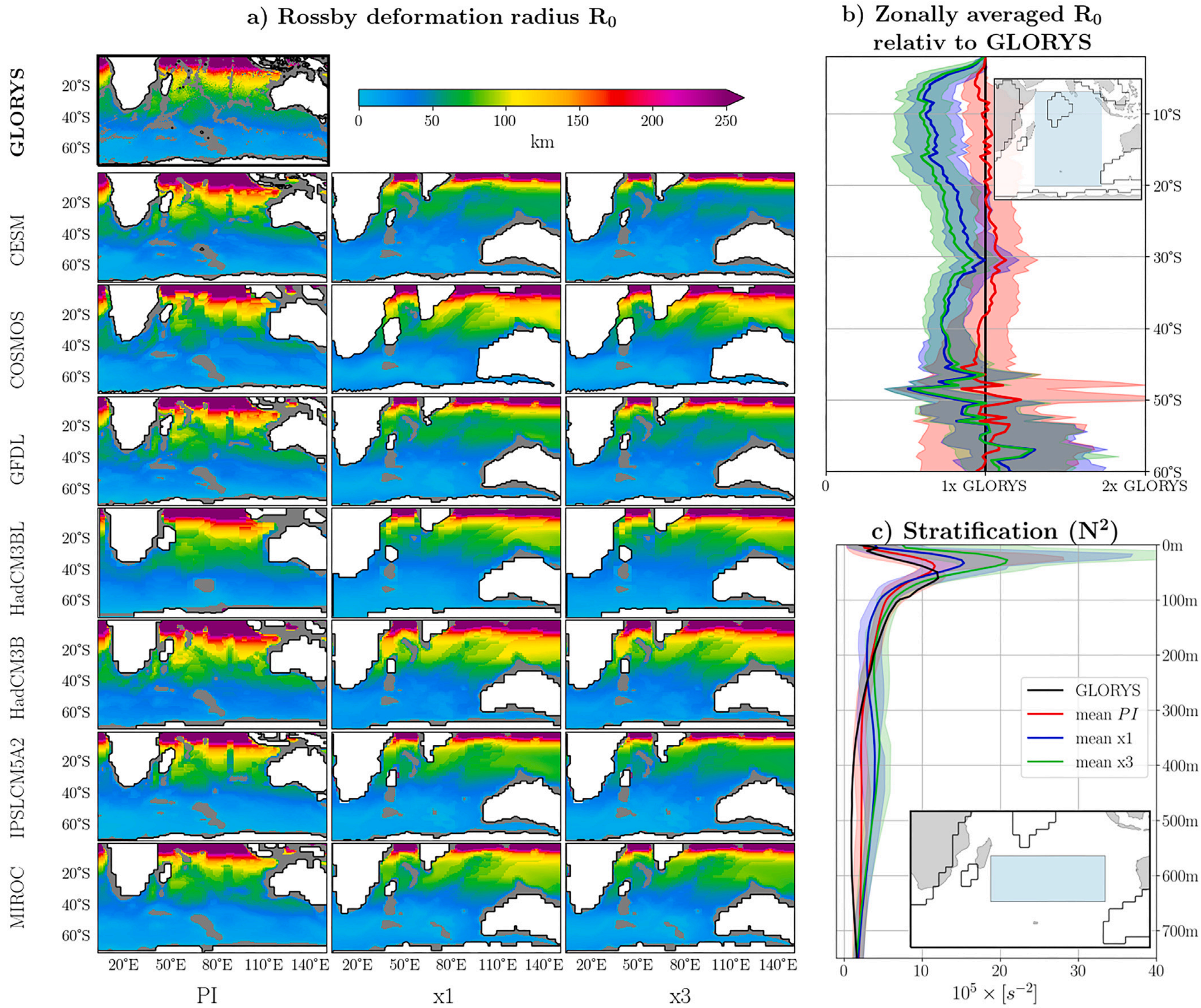

Fig. 7. (a) Rossby deformation radius (R_0) for the configuration PI, x1 and x3 of the DeepMIP models outputs and for GLORYS. Regions shallower than 2500 m are shaded in gray. (b) Zonally-averaged Rossby deformation radius over 50° E–100° E (see map) averaged over the PI configurations (red), paleo x1 CO_2 configurations (blue), and paleo x3 CO_2 configurations (green). The associated shaded areas indicate the inter-model spread.(c) Brunt–Vaisala frequency (N^2) profiles averaged in the 20° S–40° S, 50° E–100° E area (see map) averaged over the PI configurations (red), paleo x1 CO_2 configurations (blue), and paleo x3 CO_2 configurations (green). The associated shaded areas indicate the inter-model spread. (For interpretation of the references to color in this figure legend, the reader is referred to the web version of this article.)

4.6. Rossby deformation radius

Fig. 7a represents the Rossby deformation radius to investigate how the GCMs, Eocene geography and CO_2 concentrations may influence eddy size, wave propagation and length scale of baroclinic instability. Indeed, near the Agulhas Bank, the current's momentum overcomes topographic vorticity constraints when its width matches the Rossby deformation radius, causing it to detach and retroflect (Lutjeharms et al., 2003). Rossby deformation radius governs the kinetic energy cascade from the mean current to eddies. Eddies with diameters close to ~40 km dominate the Agulhas Return Current, contributing to its intense mesoscale variability (Tedesco et al., 2022). Hutchinson et al. (2018) shows that seasonal phasing of the Agulhas transport is found to be highly sensitive to baroclinic Rossby waves propagation speeds, depending directly on Rossby deformation radius. Stratification profiles (Fig. 7c) and the zonally-averaged Rossby deformation radius in the central part of the basin show that, on average, the PI simulations accurately represent Rossby deformation radius consistent with GLORYS. The differences observed are mainly due to grid differences between models which once interpolated, result in varying bathymetries.

In paleo-simulations, significant changes in terms of Rossby deformation radius should be considered relative to the position of the continents, which have shifted significantly (along with the value of the Coriolis parameter) between the PI configurations and the paleo simulations. For example, if we consider the northern region of Madagascar, where large anticyclonic eddies form (Halo et al., 2014) and currently have a strong influence on the Agulhas system, values strongly decrease from ~150 km in PI simulations to ~75 km in paleo simulations (Fig. 7a). Similarly, in the retroflection area at the southern tip of South Africa, which is particularly sensitive to mesoscale activity, Rossby deformation radius strongly decreases from ~50 km in PI simulations to ~20 km in paleo simulations. If we examine changes at a constant latitude in the SISG (Fig. 7b), particularly at low latitudes, Rossby deformation radius is lower in paleo configurations (at 10° S, PI simulations yield an average R_0 ~ 165 km compared to R_0 ~ 100 km in paleo x1 CO_2 and paleo x3 CO_2). This is mainly

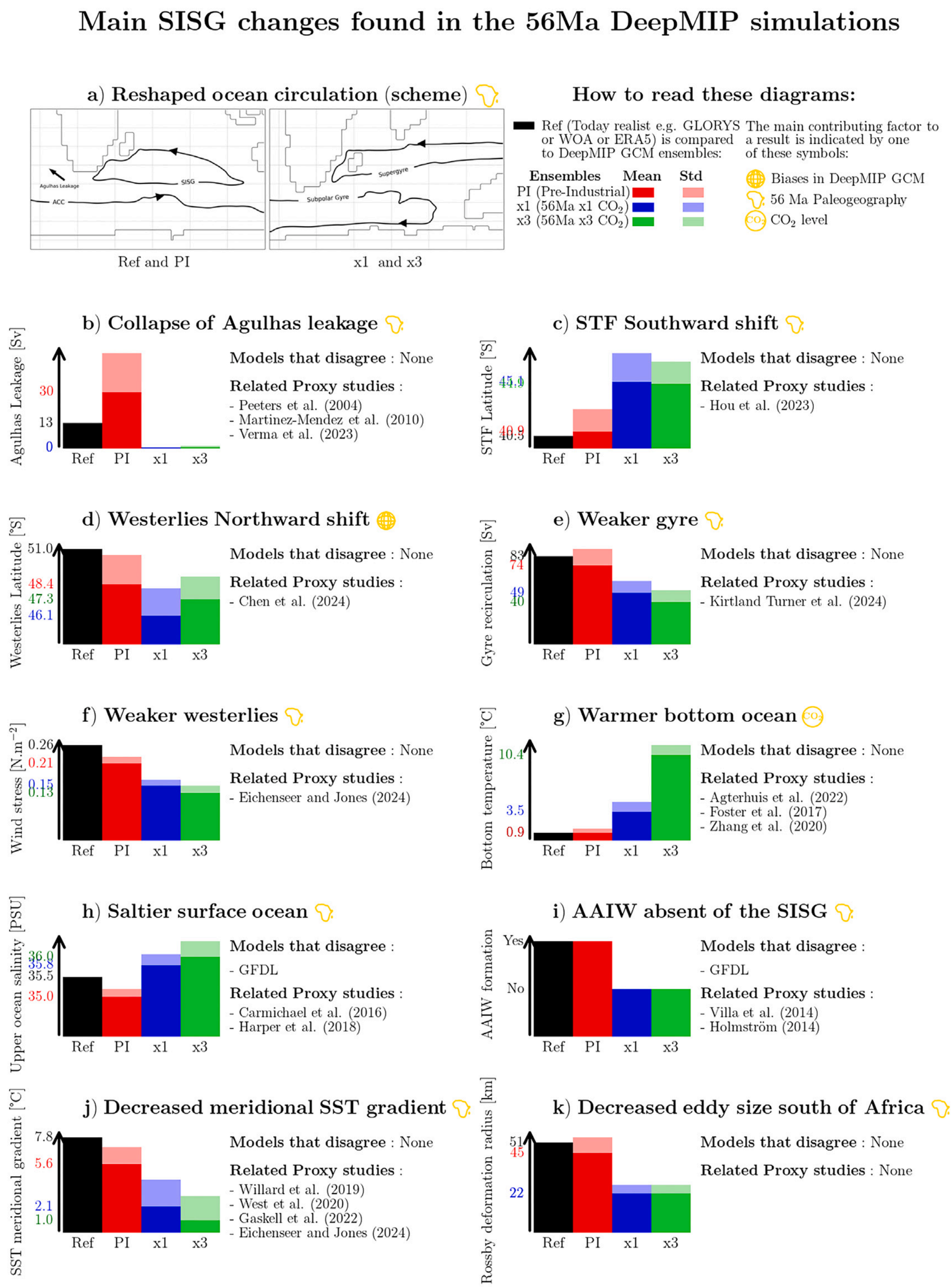

Fig. 8. Summary of the main changes found in the Eocene DeepMIP simulations, the major contributing factor (highlighted in yellow), the models that disagree and related proxy studies. The values in the "Warmer bottom ocean" panel (g) correspond to the average bottom water temperature in the characteristic gyre region (40° S–20° S, 50° E–100° E). For "Saltier surface ocean" panel (h) the values represent the maximum salinity from the salinity profiles shown in Fig. 6b. For "Decreased eddy size south of Africa" the values correspond to the Rossby deformation radius at 40° S/30° E for PI and 50° S/20° E for paleo x1 CO_2 and paleo x3 CO_2. (For interpretation of the references to color in this figure legend, the reader is referred to the web version of this article.)

due to changes in the bathymetry used, which is shallower in the Eocene configuration (Herold et al., 2014). Indeed, if we analyze the stratification profiles, the SISG is generally more stratified in paleo simulations, particularly in surface waters (Fig. 7c).

5. Discussion

5.1. Representation of the modern SISG with the DeepMIP models

The shape, intensity, and water mass composition of the South Indian subtropical Gyre in current reanalysis differ significantly from those in the Eocene DeepMIP simulations. Main results are summarized in Fig. 8: changes in the shape of the SISG (panels a, b, c, and d), changes in the intensity of gyre circulation (panels e and f), changes in the composition of water masses (panels g, h, i, and j) and potential changes in the characteristic size of eddies (panel k). Differences between today's reference reanalyses and paleo ×3 CO_2 results from a combination of factors: biases in low-resolution GCMs, the chosen Eocene geography in the DeepMIP configurations, and the CO_2 concentrations used in the simulations. Fig. 8 quantifies these differences, helping to identify their sources (main contributing factors are highlighted) and assess the reliability of these changes. However the individual contributions of model biases, paleogeography, and CO_2 forcing are not simply additive, and their combined effect may involve nonlinear interactions that we are not able to quantify within the scope of this study. In Fig. 8, we have also listed the models which deviate from the main results, as well as the referenced proxy studies related to these results (right column of each panel). Prior to assessing the influence of Eocene-specific features such as elevated CO_2 concentrations and paleogeography, it is crucial to identify the key biases arising from the models themselves. The pre-industrial (PI) simulations from the DeepMIP ensemble constitute an essential benchmark to evaluate the impact of Eocene boundary conditions on ocean circulation. It is well established that low-resolution GCMs do not explicitly resolve mesoscale turbulence, despite its dominant contribution to the oceanic kinetic energy and its central role in lateral transports of heat, salt, and buoyancy, as well as intrinsic variability (Ferrari and Wunsch, 2009; Danabasoglu et al., 2014). This limitation leads to persistent biases in western boundary currents and frontal systems, affecting air–sea exchanges and gyre strength (Danabasoglu et al., 2014; Hewitt et al., 2017), and prevents a realistic representation of submesoscale and mixed-layer processes, often resulting in overly deep mixed layers and biased vertical exchanges that are highly sensitive to numerical dissipation (Bodner et al., 2023). Deep convection, high-latitude water-mass transformation, and overflows are likewise affected. While they do not resolve mesoscale features due to their coarse resolution (2°), they still manage to reproduce key aspects of the present-day South Indian Ocean circulation. The PI simulations capture the large-scale horizontal circulation patterns of the SISG, including a well-positioned STF (Fig. 8c), delimiting the ACC to the south and the anticyclonic South Indian Subtropical Gyre system to the north. However, certain aspects such as the magnitude of the Agulhas leakage (Fig. 8b) and the overall gyre strength (Fig. 8e) exhibit substantial intermodel variability. In terms of water mass structure, the PI simulations are able to replicate the general layering and shape of temperature–salinity (Θ–S) profiles within the subtropical gyre (Fig. 4). The Antarctic Intermediate Water (AAIW), for instance, is represented in most models as a distinct low-salinity water mass subducting beneath the Subtropical Surface Water (STSW). However, salinity and temperature biases are apparent, particularly in the intermediate and deep layers, leading to a negative bias in modeled density profiles compared to WOA. Yet, some models show deviations in Rossby deformation radius due to differences in bathymetry and vertical stratification structure, which can affect the accurate simulation of western boundary current dynamics.

5.2. Transport changes

The barotropic transport streamfunction differs radically between the present day (GLORYS reanalysis) and the DeepMIP Eocene x3 CO_2 simulations. The ACC is absent in the paleo x1 CO_2 configuration and is replaced by a cyclonic subpolar gyre (Fig. 8a), due to closed Tasman Strait and Drake Passage. The position of the zero wind stress curl indicates the boundary between the subtropical gyre and the subpolar gyre and links changes in wind stress curl and transport. Several factors can explain a weak or collapsed Agulhas leakage. Rühs et al. (2022) links the modern increase in Agulhas leakage associated with climate warming to the intensification of wind stress curl in the region. In our case, under the paleo x1 CO_2 configuration, the amplitude of the wind stress curl tends to decrease (Fig. 2), which could account for a reduction in Agulhas leakage. Additionally, Verma et al. (2023), through the study of planktonic foraminifera and other proxies, show that during glacial periods, the STF shifted 7° further north, blocking the access of Indian subtropical waters to the Atlantic. In our scenario, the African continent is located 10° further south (Lotfy et al., 2017), reaching 40° S, which defines the position of the STF and effectively prevents Agulhas leakage. With the zero wind stress curl shifted northward (Fig. 8d), it moves significantly closer to the African continent, which leads to a reduction in Agulhas leakage (Sijp and England, 2008). Several other proxies have been employed to investigate past changes in the Agulhas leakage. For instance, Peeters et al. (2004) relied on planktonic foraminiferal assemblages, while Martínez-Méndez et al. (2010) used δ^{18}O and Mg/Ca ratios measured on *Globigerina bulloides* from the Agulhas corridor during glacial periods. However, such records are not available for the Eocene.

The position of the retroflection is also affected by the paleo-configuration. Indeed, Africa, which intersects the STF, prevents the retroflection from occurring south of Africa. It now takes place to the east of the African coast. A displacement of the retroflection could have substantial consequences for both oceanic and climatic conditions in the region, one of which might be its influence on the regional hydrological cycle. Njouodo et al. (2021) show that the Agulhas Current system plays a very important role in precipitation in the region. This result is also evident in Figure 4 of Williams et al. (2022), which compares precipitation patterns from the DeepMIP early Eocene simulations. For both paleo x1 CO_2 and paleo x3 CO_2 scenarios, southern Africa experiences reduced precipitation, whereas the ocean to the east of the continent where the retroflection is now located shows increased precipitation (except in the GFDL model).

The primary factor explaining the reduction in transport (Fig. 8e) is the paleogeographic change in the Eocene, but the increase in CO_2 also induces a further decrease in the gyre transport from an average of 48.6 Sv in the paleo x1 CO_2 simulations to 39.9 Sv in the paleo x3 CO_2 simulations. This corresponds to a reduction comparable to the decrease in the intensity of the wind stress curl of the westerlies, suggesting that the subtropical gyre circulation during the Eocene was primarily Sverdrupian i.e., driven by the balance between wind stress curl and the meridional transport of water as described by Sverdrup theory (Sverdrup, 1947), a feature that is also observed in the present day (Penven et al., 2021). Kirtland Turner et al. (2024) demonstrate, using benthic foraminiferal $\delta^{13}C$ and $\delta^{18}O$ records along with an intermediate-complexity model, that overturning circulation in the Southern Hemisphere declined during the Early Eocene.

The Eocene x3 CO_2 simulation shows that the STF is located 4.4° further south compared to the present-day position. As with other features, the Eocene geography is the primary driver of this shift (see Fig. 8), while CO_2 only induces a minor southward displacement of 0.2°. Studying proxies including dinoflagellate cyst biogeography and benthic foraminiferal clumped isotopes from offshore Tasmania, Hou et al. (2023) suggest that during the Eocene, the STF was located even farther south (53° S) before migrating northward between 14 Ma and 7 Ma to its present-day position around 40° S. This suggests that models may underestimate the southward shift. De Boer et al. (2013) show that this southward shift of the STF is not incompatible with the northward migration of the westerlies (51° S to 47.3° S) and that the STF position is primarily controlled by topography, explaining why geographic changes remain the dominant factor in its displacement.

5.3. Water masses changes

We have observed that water masses are also profoundly affected in these different simulations. The Eocene is known for its warmer oceans compared to the present day. In our study region and for our simulations, this warming is particularly striking at depth. The average bottom temperature over our characteristic gyre region (50° E–100° E, 20° S–40° S) increases from 0.9 °C in WOA to 10.4 °C in the Eocene x3 CO_2 simulations (Fig. 8g). Our findings are consistent with those of Zhang et al. (2020), who estimated a similar deep-water temperature increase of this magnitude using Mg/Ca ratios. This is also in line with Agterhuis et al. (2022) which measured stable and agglomerated isotopes by combining carbonate clumped isotope thermometer (Δ_{47}) measurements from different benthic species, obtaining temperatures during hyperthermal events ranging from 13 °C to 17 °C. More broadly, compilations of long-term CO_2 reconstructions demonstrate that such elevated greenhouse gas levels are sufficient to maintain substantially warmer deep-ocean conditions over geological timescales (Foster et al., 2017). While this temperature change is primarily driven by the increase in CO_2, geography also plays a significant role, accounting for 27% of the warming, in contrast to the PI simulations, which yield bottom temperatures identical to WOA. This effect could be attributed to the closure of major oceanic gateways, which has been shown to strongly modulate ocean circulation and deep-water properties in Eocene boundary condition experiments (Toumoulin et al., 2020).

Keeping in mind the sea surface/subsurface salinity model intervariability, the maximum salinity (around 200 m depth) in the sections of our study region (Fig. 6b and Fig. 8h) increases by 0.5 PSU between WOA and the Eocene x3 CO_2 simulations. Once again, geographical changes appear to be the primary driver of this result. A saltier Indian Ocean during the Eocene is also supported by proxy data. At Ocean Drilling Program (ODP) Site 1209 in the Pacific, which provides insights into broader tropical ocean patterns, including the Indian Ocean, an increase in Sea Surface Salinity (SSS) during the Paleocene-Eocene Thermal Maximum was found (Harper et al., 2018; Carmichael et al., 2016). These studies, combining model comparisons and proxy data, demonstrate a global intensification of the hydrological cycle, with significantly higher evaporation–precipitation (E-P) values between 0° S and 40° S. It is noteworthy that orbital cycles, which remain unchanged in this case, also played a significant role in shaping hydrological cycles, as highlighted by Briard (2020). Further sensitivity tests would be necessary to fully understand the exact role of geography in the observed salinity increase.

The temperature gradient between low and high latitudes is significantly affected in the Eocene x3 CO_2 configurations (Fig. 8j) compared to the present day, decreasing from 27.8 °C in WOA to 21 °C in x3 CO_2. Numerous proxy sources, including leaf assemblages, floristic composition, as well as $\delta^{18}O$ isotopes in planktonic and benthic foraminifera, support this result (Willard et al., 2019; West et al., 2020; Eichenseer and Jones, 2024; Gaskell et al., 2022). This result, known as polar amplification, is also observed in current climate change, where the Arctic is warming on average four times faster than the global climate, and Antarctica three times faster (Rantanen et al., 2022; Clem et al., 2020). In the past, this phenomenon was further amplified by paleogeography. Indeed, with closed oceanic gateways, the meridional heat transport was significantly enhanced (Zhang et al., 2020).

All DeepMIP models are able to generate AAIW in the PI simulations characterized by a freshwater peak around the isopycnal 1036 kg m^{-3} in Fig. 4. They do not exhibit any evidence of AAIW formation in the paleo x1 CO_2 and paleo x3 CO_2 simulations, except for GFDL. The strong westerlies driving the Antarctic Circumpolar Current (ACC) generate equatorward Ekman transport, which plays a crucial role in the formation of AAIW. This process pushes surface waters away from Antarctica, contributing to the Antarctic Divergence region and inducing the upwelling of deep water, which subsequently subducts beneath the subtropical surface water, forming AAIW (Sallée et al., 2010). Around 42 Ma, a significant shift occurred in the Indian Ocean, leading to a divergence in $\delta^{18}O$ values (Holmström, 2014) between its northern and southern regions. This divergence suggests the emergence of a thermal segregation of intermediate water masses, resulting in two distinct water bodies: the cool, high-latitude AAIW and a warm, low-latitude water mass known as Tethyan-Indian Saline Water (TISW). This phenomenon is believed to be linked to the formation of the ACC and the cooling of high-latitude temperatures, which allowed intermediate waters to sink more extensively than before, forming the cool water mass on a larger scale. Further evidence of this thermal segregation is provided by changes in the distribution of planktonic and benthic foraminifera, as well as a marked retreat of warm water calcareous nannoplankton in the southern Indian Ocean (Villa et al., 2014).

5.4. Wind changes

DeepMIP simulations under Eocene conditions (CO_2 concentrations and paleogeography), represented in the paleo x3 CO_2 and paleo x1 CO_2 configurations, indicate a northward shift and weakening of the westerly winds compared to the modern situation (ERA5 reanalysis). This shift differs from the findings of Chen et al. (2024), who suggested a more southerly position of the westerlies during the Eocene, based on neodymium and hafnium isotopic ratios and clay mineralogy extracted from the U1514 site in the Mentelle Basin. While the weakening wind stress curl is not directly measured in proxies, Eichenseer and Jones (2024) investigated this aspect using geochemical proxies combined with ecological data from mangrove communities and coral reefs. Their study estimated a flattened latitudinal sea surface temperature (SST) gradient of 13.3 °C. In contrast, DeepMIP simulations give an average SST gradient of 21 °C (Fig. 8j), which remains lower than the present-day gradient of 27.8 °C observed in WOA. This reduction in the SST gradient, when applied to the thermal wind balance, leads to a weakened westerly wind system. The lower meridional temperature gradient results in reduced Sea Level Pressure (SLP) over Antarctica compared to stronger mid-latitude SLP, thereby driving a poleward shift of the westerlies. This mechanism is currently observed in global warming scenarios and is associated with the positive phase of the Southern Annular Mode (SAM) (Marshall, 2003). As indicated in Fig. 8, the most significant shift (2.6°) in the position and intensity of the westerlies occurs in the ERA5/PI comparison. This suggests that the primary driver of the westerly wind shift is the PI models biases. Therefore, this result should be interpreted with caution. Nevertheless, we still obtain a northward shift of the westerlies between PI and paleo x1/x3 CO_2. Similarly, Abhik et al. (2024) found that monsoonal changes were predominantly controlled by paleogeographic factors, with atmospheric CO_2 playing a minor role. Our results also indicate a stronger influence of paleogeography compared to atmospheric CO_2 concentrations. These important PI model biases, with strong intermodel variability, can be attributed to various factors, including the parameterization of atmospheric turbulent fluxes, heat and moisture exchanges, coupling realism, model resolution, cloud parameterization, and surface albedo representation. Additionally, pre-industrial simulations are performed with lower atmospheric CO_2 concentrations than ERA5, which may contribute to the observed shift. Indeed, ongoing global warming is causing a poleward shift and intensification of the Southern Hemisphere westerlies (Tim et al., 2019; Perren et al., 2020).

5.5. High resolution paleoceanographic perspectives

A smaller Rossby deformation radius, as observed in the paleoclimate simulations for the Eocene (paleo x1 CO_2 and paleo x3 CO_2 in Fig. 7b), could significantly impact ocean dynamics in the region. The Rossby deformation radius sets the size and propagation speed of Rossby waves and eddies. Outside the equatorial band, Chelton et al. (1998) defines the Rossby deformation radius (λ_m) associated with mode-m as $\lambda_m = \frac{c_m}{f}$, where c_m is the phase speed of gravity waves for mode-m and f is the coriolis parameter. The magnitude of this radius is critical for many oceanic processes.

Chelton et al. (2011) demonstrated that smaller eddies (corresponding to a smaller Rossby deformation radius) dissipate more rapidly, leading to enhanced energy dissipation via friction and turbulent mixing. When the Rossby deformation radius is smaller, the propagation speed of first-mode baroclinic Rossby waves decreases. This implies that wind anomalies take longer to influence ocean circulation because pycnocline adjustment through these waves becomes slower. Hutchinson et al. (2018) showed that the seasonal phasing of the Agulhas Current is strongly dependent on this propagation speed: when baroclinic waves propagate more slowly, the current's response to atmospheric forcing is delayed. They also showed that signals from distant winds tend to dissipate before reaching the western boundary of the basin, mainly due to destructive interference between local wind anomalies and those propagating from the east. In a context of a smaller Rossby deformation radius, the current's response would thus be even more confined to local or near-field forcing, as long-distance communication via Rossby waves would be further inhibited. This restricts the influence of remote winds and strengthens the direct role of regional winds in modulating western boundary circulation variability.

Theiss (2004) showed that there exists a critical latitude defined by the ratio r between the Rossby deformation radius and the Rhines scale: $L_R = \sqrt{\frac{U}{\beta}}$, where U is the characteristic turbulent velocity and β is the meridional gradient of the Coriolis parameter. When $r > 1$ (at low latitudes), Rossby waves dominate and induce anisotropy by organizing the flow into alternating zonal jets. For $r < 1$, Rossby waves are less effective at structuring the flow, resulting in isotropic turbulence dominated by vortices. In practice, the critical latitude (where $r = 1$) is estimated to lie between 10° and 20° latitude (Halo et al., 2023). A smaller Rossby deformation radius would shift the condition $r = 1$ to lower latitudes. This means that zonal structures, such as alternating jets, become confined to lower latitudes, while isotropic, vortex-dominated turbulence extends closer to the equator.

Western boundary currents balance the transport of subtropical gyres in a boundary layer often associated with topography (Hughes, 2000; Gula et al., 2015). Nevertheless, frontal arguments have been put forward to link their width with the Rossby deformation radius (Saenko, 2006). As a consequence a smaller Rossby deformation radius should make western boundary currents narrower, more intense (to maintain the necessary transport) and more stable (Saenko, 2006). Chelton et al. (1998) also showed that mesoscale variability and the width of currents are directly linked to the geographical distribution of the Rossby deformation radius.

For modeling the mesoscale structures of the Agulhas Current in a paleo context, it is useful to compare Rossby deformation radius south of the Agulhas Bank. From GLORYS reanalysis, Rossby deformation radius is estimated around 51 km, whereas in the Eocene x3 CO_2 simulations, estimates are around 22 km (Fig. 8k). This difference is particularly significant, because Africa was about 10° further south during the Eocene (Lotfy et al., 2017), and Rossby deformation radius decreases with latitude. According to Soufflet et al. (2016), simulations with model based on high order numerics require at least a resolution seven times finer than the scale of the phenomenon to be properly resolved. Thus, for a Rossby deformation radius of 22 km (assuming structures span approximately $2R_0$), a resolution of around 6 km is needed to adequately resolve mesoscale features in Eocene simulations. By contrast, for the present-day Rossby deformation radius of 51 km, a resolution of about 14 km is required.

Importantly, these requirements are far finer than the ocean grid spacing used in the DeepMIP coupled simulations analyzed here. Consequently, the present DeepMIP simulations cannot resolve mesoscale vortices, ring shedding, or the associated kinetic energy cascade in the Agulhas system, and they are therefore likely to significantly underestimate the eddy kinetic energy as well as the associated temporal and spatial variability during the Eocene. The Rossby deformation radius–based arguments presented above should therefore be regarded as a physically grounded indication of how the unresolved mesoscale regime may differ under Eocene boundary conditions, since the dynamical consequences of a reduced Rossby deformation radius cannot be captured by the current low-resolution models.

In order to resolve the mesoscale processes of the Agulhas Current system, Le Hir et al. (2024) conducted a sensitivity test of ocean circulation in the southwestern Indian Ocean to the closure of the Mozambique Channel, which may have occurred intermittently during the Cenozoic (Masters et al., 2021; Aslanian et al., 2023), using a model with horizontal resolution of 1/12° (i.e. about 9 km). However, Le Hir et al. (2024) remains an idealized study and cannot be considered as a paleoclimatic experiment, as large-scale boundary conditions and atmospheric forcing were unchanged. Results we obtained here will serve as a preliminary step in identifying robust patterns and the biases inherent in GCMs in their representation of the large-scale SISG in the Eocene. Le Hir et al. (2024) provides insights into the tools to apply the sensitivity test of ocean circulation in the southwestern Indian Ocean to the closure of the Mozambique Channel in a paleoclimatic context. Given Rossby deformation radius relative to Africa's position, eddy-resolving regional simulations in the Eocene configuration would require a finer resolution than for the present to resolve explicitly the mesoscale processes.

6. Conclusion

The South Indian Subtropical Gyre during the Early Eocene was substantially different from its modern configuration. Simulations from the DeepMIP project show a weaker, restructured gyre extending into the Pacific, bordered in the south by a subpolar gyre replacing today's Antarctic Circumpolar Current and at North by a tropical gyre, disconnected from the Atlantic due to the collapse of the Agulhas leakage, and a poleward-shifted STF. Despite limitations of these low-resolution General Circulation Models, DeepMIP models consistently reproduce key features mainly supported by proxy data studies, such as warmer deep waters, a reduced meridional temperature gradient, the disappearance of Antarctic Intermediate Water (AAIW), and altered wind patterns. The dominant influence of Eocene paleogeography, especially the closure of ocean gateways and the southward shift of the African continent, emerges as the main driver of these changes, more than CO_2 influence. Overall, the results provide robust insights into past ocean dynamics and lay the groundwork for future studies that aim to refine our understanding of the ocean circulation under past climate conditions.

CRediT authorship contribution statement

Théo Le Hir: Writing – review & editing, Writing – original draft, Visualization, Validation, Methodology, Investigation, Formal analysis, Conceptualization. **Pierrick Penven:** Writing – review & editing, Visualization, Validation, Supervision, Methodology, Formal analysis. **Thierry Huck:** Writing – review & editing, Visualization, Validation, Supervision, Methodology, Investigation. **Maryline Moulin:** Writing – review & editing, Supervision, Project administration, Funding acquisition. **Marina Rabineau:** Writing – review & editing, Supervision, Project administration, Funding acquisition. **Daniel Aslanian:** Writing – review & editing, Visualization, Validation, Supervision, Methodology, Investigation.

Declaration of competing interest

The author and co-authors declare that they have no known competing financial interests or personal relationships that could have appeared to influence the work reported in this paper.

Appendix A. Method to compute the barotropic streamfunction

ψ represents the depth-integrated horizontal mean flow in the ocean and reflects the position, strength, and connections of the gyre with other basins. It represents the mean transport associated with the large-scale circulation. The streamfunction can be derived from the Helmholtz decomposition, which states that any vector field can be decomposed into an irrotational (divergent) component and a non-divergent (rotational) component:

$$\mathbf{u} = \nabla \times \psi + \nabla \phi,$$

where $\nabla \times \psi$ is the rotational (non-divergent) component and $\nabla \phi$ is the irrotational (divergent) component. Taking the curl of the barotropic velocity field yields:

$$\Delta \psi = \nabla \times \mathbf{u} = \zeta$$

where ζ is the vorticity of the vertically integrated currents, $\zeta = \partial_x V - \partial_y U$. The following method is applied to invert the Laplacian and compute ψ:

1. Verify that the fluxes of U and V are globally conserved over the selected domain (here encompassing the SISG). If not, u and v are adjusted to enforce global mass flux conservation along the domain boundaries.
2. Compute ψ at the boundaries from U and V. Propagate ψ across the land mask, ensuring that ψ remains constant along solid boundaries (no flux through land).
3. Identify and label connected regions (e.g., islands) in a binary mask by assigning a unique integer to each contiguous group of land masks elements based on specified connectivity.
4. Since the problem is linear, the solution can be expressed following Colin de Verdière and Ollitrault (2016) as:

$$\psi = \psi_0 + \sum_{k=1}^{N} \mu_k \psi_k$$

where:

- ψ_0 is the circulation on the entire domain, it is the particular solution of the Poisson equation $\Delta\psi_0 = \nabla \times \mathbf{u}$, with zero Dirichlet boundary conditions on the external boundary and on all islands ($\psi_0 = 0$).
- ψ_k is the circulation associated with island k, it is the homogeneous solution satisfying $\Delta\psi_k = 0$, with $\psi_k = 1$ on island k and $\psi_k = 0$ on all other boundaries and islands.

ψ_0 and ψ_k are determined by applying a successive over-relaxation method (Yang and Matthias, 2007) to invert the Laplacian. The coefficients μ_k are determined to ensure that the circulation around each island (defined by the contour ∂I_k) matches the circulation derived from the barotropic transport field $\mathbf{u}$:

$$\underbrace{\oint_{\partial I_k} \mathbf{u} \cdot \mathbf{n}\, ds}_{\text{Circulation around island } k} = \underbrace{\oint_{\partial I_k} \partial_n \psi_0\, ds}_{\text{Contribution from } \psi_0} + \sum_{j=1}^{N} \mu_j \underbrace{\oint_{\partial I_k} \partial_n \psi_j\, ds}_{\text{Contribution of each islands}}$$

This forms a linear system, for k = 1, …, N:

$$\sum_{j=1}^{N} A_{kj}\, \mu_j = b_k$$

with:

$$A_{kj} = \oint_{\partial I_k} \partial_n \psi_j\, ds, \quad b_k = \oint_{\partial I_k} \mathbf{u} \cdot ds - \oint_{\partial I_k} \partial_n \psi_0\, ds$$

Solving this system yields the coefficients μ_k, from which the complete streamfunction ψ can be reconstructed to satisfy both the vorticity constraint and the correct circulation around each island.

This method ensures that the streamfunction accurately represents the circulation around each island in the domain, as imposed by the barotropic transport field.

With the exception of IPSL-CM5A2, the models provide an output variable for the barotropic streamfunction ("msftbarot"), as described in the CMIP6 documentation (Griffies et al., 2014). This variable is computed by vertically integrating the zonal mass transport (ρu) over the entire water column and then meridionally integrating this transport from Antarctica. The method we propose, ensures a dynamically consistent circulation by explicitly enforcing mass conservation at the boundaries of the domain. This distinction is particularly important in our study, as the u and v velocity fields are interpolated onto a common, finer grid across all simulations in order to compute and compare key metrics of Agulhas leakage. As shown in Fig. A.1, the choice of method has little impact on the pre-industrial simulations of MIROC. In contrast, for HadCM3B, the Antarctic Circumpolar Current transport is reduced, and the gyre recirculation is approximately 15 Sv weaker. These differences may have several sources. First, the archived u and v fields are temporally averaged, whereas "msftbarot" is diagnosed directly within the model. Second, the interpolation of the velocity fields onto a common grid may introduce small local inconsistencies in the vertically integrated transport. In a cumulative integration, such small differences can accumulate with distance from the southern boundary, leading to discrepancies in the reconstructed streamfunction even when the underlying model solution itself is mass-conserving. In this context, the Laplacian-inversion/Helmholtz approach is used not because the model transport is not mass-conserving, but because it provides a robust and numerically controlled diagnostic of the barotropic circulation that is less sensitive to the direction of integration and better suited for intercomparison across models with different grids and geometries.

Appendix B. Method to compute the Agulhas leakage

Because of the coarse resolution of the paleoclimate simulations, the Agulhas Leakage cannot be associated with eddies, allowing the use of the mean transport function ψ to evaluate its intensity. This is achieved by specifically separating the streamlines ending in the Atlantic Ocean (i.e. defining the Leakage) to the one participating to the Agulhas retroflection and to the Antarctic Circumpolar Current. Since we have defined the value of ψ to be zero over the African continent, this is practically achieved by selecting and summing contours spaced at 0.1 Sv that satisfy the following conditions (summarized in Fig. B.1):

- **STF**: crosses both the Good Hope Line and the 40° E section north of the STF. This condition excludes contours associated with ACC counter-currents.
- **GHL**: connects the Good Hope Line (GHL) at 0° E, as defined by Gladyshev et al. (2008). This condition ensures that the contour enters the Atlantic Ocean and eliminates local recirculations associated with the Agulhas retroflection and the Agulhas Subgyre when computing the leakage.
- **40° E**: connects to the meridional section at 40° E, as defined by Stramma and Lutjeharms (1997). This condition ensures that the contour originates from the Indian Ocean.
- **East → West**: this condition is satisfied if the contour connects first to 40° E and then to the GHL. It confirms that the barotropic flow along the contour goes from the Indian Ocean to the Atlantic.

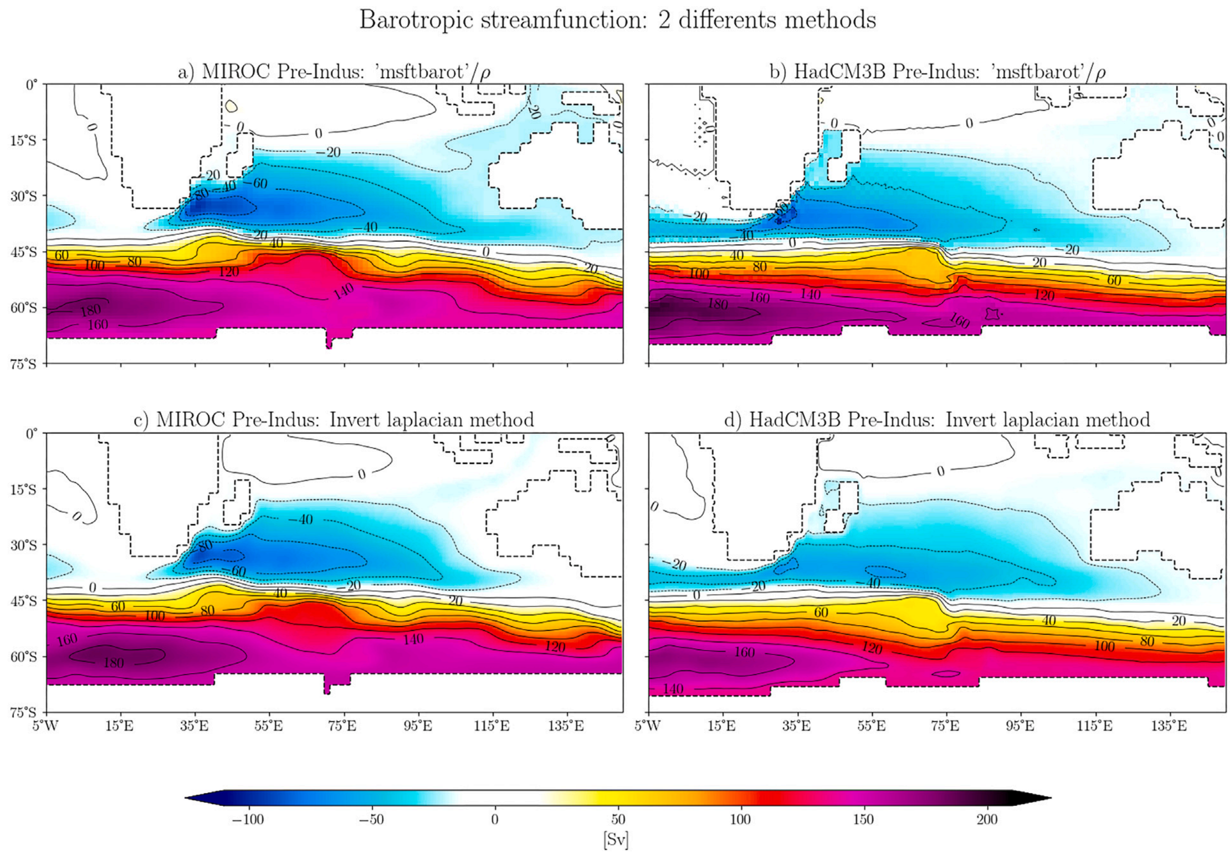

Fig. A.1. Barotropic streamfunction for the pre-industrial (PI) simulations of the MIROC and HadCM3B models, computed using two different methods: derived from the "msftbarot" in panels (a) and (b), and obtained by inverting a Laplacian in panels (c) and (d).

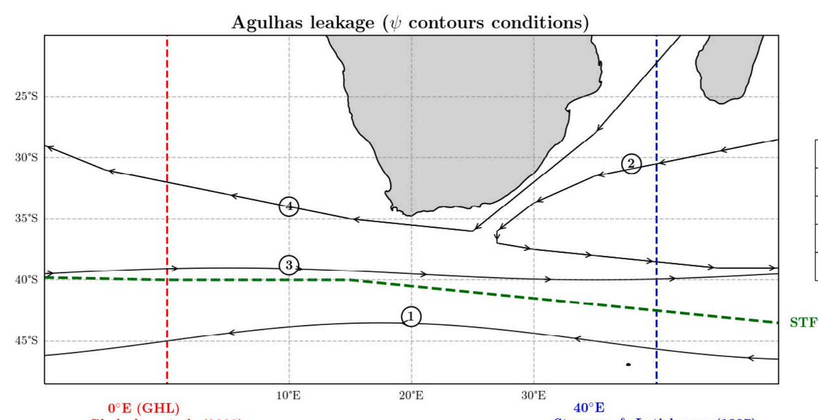

ψ contours	STF	GHL	40°E	Est→Ouest
1	×	✓	✓	✓
2	✓	×	✓	×
3	✓	✓	✓	×
4	✓	✓	✓	✓

Fig. B.1. Schematic representation of the barotropic streamfunction (ψ) contours used to compute Agulhas leakage. Four example contours are shown, each representing different combinations of the conditions required to qualify as leakage pathways. These conditions include being northward of the Subtropical Front (STF), connecting to the Good Hope Line (GHL), connecting the 40° E meridional section, and exhibiting an east-to-west direction from the Indian Ocean to the Atlantic. Contours are labeled (1–4), with arrows indicating flow direction. The table on the right summarizes which conditions are fulfilled by each contour.

By applying this method to the annually-averaged GLORYS horizontal transport, we obtain 13.1 Sv, which is close to the value obtained with the Lagrangian method applied to observations (Richardson, 2007) and from eddy resolving simulations (Schmidt et al., 2021).

Data availability

Feel free to ask for any Python diagnostics I used to perform the analyses necessary for this article.

References

Abhik, S., Capitanio, F.A., Dommenget, D., Goswami, B., Farnsworth, A., Hutchinson, D.K., Arblaster, J.M., Lunt, D.J., Steinig, S., 2024. Unraveling weak and short south Asian wet season in the early eocene warmth. Commun. Earth Environ. 5 (1), 133.

Agterhuis, T., Ziegler, M., de Winter, N.J., Lourens, L.J., 2022. Warm deep-sea temperatures across eocene thermal maximum 2 from clumped isotope thermometry. Commun. Earth Environ. 3 (1), 39.

Aslanian, D., Pellen, R., Rabineau, M., Moulin, M., Leroux, E., Delaunay, A., Baby, G., Courgeon, S., Linol, B., Suc, J.-P., et al., 2023. The postulation of intermittent land bridges as an explanation for reiterated colonization events of Madagascar by

African vertebrates: An in-depth review and novel insights in honour of the late Judith Masters and Fabien Génin. Earth-Sci. Rev. 246, 104585.
Beal, L.M., De Ruijter, W.P., Biastoch, A., Zahn, R., 2011. On the role of the Agulhas system in ocean circulation and climate. Nature 472 (7344), 429–436.
Beal, L.M., Elipot, S., Houk, A., Leber, G.M., 2015. Capturing the transport variability of a western boundary jet: Results from the agulhas current time-series experiment (ACT). J. Phys. Oceanogr. 45 (5), 1302–1324.
Belkin, I.S., Levitus, S., Antonov, J., Malmberg, S.-A., 1998. Great salinity anomalies in the north atlantic. Prog. Oceanogr. 41, 1–68.
Bodner, A., Balwada, D., Zanna, L., 2023. A data-driven approach for parameterizing submesoscale vertical buoyancy fluxes in the ocean mixed layer. J. Adv. Model. Earth Syst. 17 (4), e2025MS004991.
Briard, J., 2020. Expressions des grands changements paléoclimatiques au Cénozoïque (transition Eocène-Oligocène" EOT"; Miocène moyen" MMCO, chsep=, midc=(Ph.D. thesis), MMCT") en domaine côtier à partir de la géochimie des bivalves. Université Paul Sabatier-Toulouse III, France.
Carmichael, M.J., Lunt, D.J., Huber, M., Heinemann, M., Kiehl, J., LeGrande, A., Loptson, C.A., Roberts, C.D., Sagoo, N., Shields, C., et al., 2016. A model–model and data–model comparison for the early Eocene hydrological cycle. Clim. the Past 12 (2), 455–481.
Chapman, P., Di Marco, S., Davis, R., Coward, A., 2003. Flow at intermediate depths around madagascar based on ALACE float trajectories. Deep. Sea Res. Part II: Top. Stud. Ocean. 50 (12–13), 1957–1986.
Chelton, D.B., DeSzoeke, R.A., Schlax, M.G., El Naggar, K., Siwertz, N., 1998. Geographical variability of the first baroclinic rossby radius of deformation. J. Phys. Oceanogr. 28 (3), 433–460.
Chelton, D.B., Esbensen, S.K., Schlax, M.G., Thum, N., Freilich, M.H., Wentz, F.J., Gentemann, C.L., McPhaden, M.J., Schopf, P.S., 2001. Observations of coupling between surface wind stress and sea surface temperature in the eastern tropical Pacific. J. Clim. 14 (7), 1479–1498.
Chelton, D.B., Schlax, M.G., Samelson, R.M., 2011. Global observations of nonlinear mesoscale eddies. Prog. Oceanogr. 91 (2), 167–216.
Chelton, D.B., Schlax, M.G., Samelson, R.M., de Szoeke, R.A., 2007. Global observations of large oceanic eddies. Geophys. Res. Lett. 34 (15), L15606.
Chen, H., Xu, Z., Bayon, G., Fan, Q., Pogge von Strandmann, P.A., Wang, W., Sun, T., Li, T., 2024. Meridional shifts of the southern Hemisphere westerlies during the early Cenozoic. Geophys. Res. Lett. 51 (13), e2024GL110182.
Clem, K.R., Fogt, R.L., Turner, J., Lintner, B.R., Marshall, G.J., Miller, J.R., Renwick, J.A., 2020. Record warming at the south pole during the past three decades. Nat. Clim. Chang. 10 (8), 762–770.
Colin de Verdière, A., Ollitrault, M., 2016. A direct determination of the world ocean barotropic circulation. J. Phys. Oceanogr. 46 (1), 255–273.
Cramwinckel, M.J., Burls, N.J., Fahad, A.A., Knapp, S., West, C.K., Reichgelt, T., Greenwood, D.R., Chan, W.-L., Donnadieu, Y., Hutchinson, D.K., et al., 2023. Global and zonal-mean hydrological response to early eocene warmth. Paleoceanogr. Paleoclimatology 38 (6), e2022PA004542.
Cramwinckel, M.J., Woelders, L., Huurdeman, E.P., Peterse, F., Gallagher, S.J., Pross, J., Burgess, C., Reichart, G.-J., Sluijs, A., Bijl, P.K., 2020. Surface-circulation change in the southern ocean across the middle eocene climatic optimum: inferences from dinoflagellate cysts and biomarker paleothermometry. Clim. Past 16, 1667–1689.
Danabasoglu, G., Yeager, S.G., Bailey, D., Behrens, E., Bentsen, M., Bi, D., Biastoch, A., Böning, C., Bozec, A., Canuto, V.M., et al., 2014. North atlantic simulations in coordinated ocean-ice reference experiments phase II (CORE-II). Part I: mean states. Ocean. Model. 73, 76–107.
De Boer, A.M., Graham, R.M., Thomas, M.D., Kohfeld, K.E., 2013. The control of the southern hemisphere westerlies on the position of the subtropical front. J. Geophys. Res.: Ocean. 118 (10), 5669–5675.
De Ruijter, W., 1982. Asymptotic analysis of the agulhas and Brazil current systems. J. Phys. Oceanogr. 12 (4), 361–373.
Dencausse, G., Arhan, M., Speich, S., 2011. Is there a continuous subtropical front south of Africa? J. Geophys. Res.: Ocean. 116 (C2).
Dijkstra, H.A., De Ruijter, W.P., 2001. On the physics of the agulhas current: Steady retroflection regimes. J. Phys. Oceanogr. 31 (10), 2971–2985.
Donohue, K.A., Tracey, K., Watts, D.R., Chidichimo, M.P., Chereskin, T., 2016. Mean antarctic circumpolar current transport measured in drake passage. Geophys. Res. Lett. 43 (22), 11–760.
Edgar, K.M., Anagnostou, E., Pearson, P.N., Foster, G.L., 2015. Assessing the impact of diagenesis on δ11b, δ13C, δ18o, Sr/Ca and B/Ca values in fossil planktic foraminiferal calcite. Geochim. Cosmochim. Acta 166, 189–209.
Eichenseer, K., Jones, L.A., 2024. Bayesian multi-proxy reconstruction of early eocene latitudinal temperature gradients. Clim. Past 20 (2), 349–362.
Eyring, V., Bony, S., Meehl, G.A., Senior, C.A., Stevens, B., Stouffer, R.J., Taylor, K.E., 2016. Overview of the coupled model intercomparison project phase 6 (CMIP6) experimental design and organization. Geosci. Model. Dev. 9 (5), 1937–1958.
Fairbridge, R.W., 2005. Ferrel cell. In: Encyclopedia of World Climatology. Springer, 378–378.
Ferrari, R., Wunsch, C., 2009. Ocean circulation kinetic energy: Reservoirs, sources, and sinks. Annu. Rev. Fluid Mech. 41 (1), 253–282.
Foster, G.L., Royer, D.L., Lunt, D.J., 2017. Future climate forcing potentially without precedent in the last 420 million years. Nat. Commun. 8 (1), 14845.
Gaskell, D.E., Huber, M., O'Brien, C.L., Inglis, G.N., Acosta, R.P., Poulsen, C.J., Hull, P.M., 2022. The latitudinal temperature gradient and its climate dependence as inferred from foraminiferal δ18o over the past 95 million years. Proc. Natl. Acad. Sci. 119 (11), e2111332119.
Gladyshev, S., Arhan, M., Sokov, A., Speich, S., 2008. A hydrographic section from South Africa to the southern limit of the antarctic circumpolar current at the greenwich meridian. Deep. Sea Res. Part I: Ocean. Res. Pap. 55 (10), 1284–1303.
Griffies, S.M., Adcroft, A.J., Balaji, V., Danabasoglu, G., Durack, P.J., Gleckler, P.J., Gregory, J.M., Krasting, J.P., McDougall, T.J., Stouffer, R.J., et al., 2014. Sampling the physical ocean in CMIP6 simulations. CLIVAR Rep..
Gula, J., Molemaker, M.J., McWilliams, J.C., 2015. Gulf stream dynamics along the southeastern US seaboard. J. Phys. Oceanogr. 45 (3), 690–715.
Halo, I., Backeberg, B., Penven, P., Ansorge, I., Reason, C., Ullgren, J., 2014. Eddy properties in the mozambique channel: A comparison between observations and two numerical ocean circulation models. Deep. Sea Res. Part II: Top. Stud. Ocean. 100, 38–53.
Halo, I., Raj, R.P., Korosov, A., Penven, P., Johannessen, J.A., Rouault, M., 2023. Mesoscale variability, critical latitude and eddy mean properties in the tropical south-east atlantic ocean. J. Geophys. Res.: Ocean. 128 (3), e2022JC019050.
Harms, N.C., Lahajnar, N., Gaye, B., Rixen, T., Dähnke, K., Ankele, M., Schwarz-Schampera, U., Emeis, K.-C., 2019. Nutrient distribution and nitrogen and oxygen isotopic composition of nitrate in water masses of the subtropical southern Indian ocean. Biogeosciences 16 (13), 2715–2732.
Harper, D.T., Zeebe, R., Hönisch, B., Schrader, C.D., Lourens, L.J., Zachos, J.C., 2018. Subtropical sea-surface warming and increased salinity during eocene thermal maximum 2. Geology 46 (2), 187–190.
Hasselmann, K., 1991. Ocean circulation and climate change. Tellus A 43 (4), 82–103.
Herold, N., Buzan, J., Seton, M., Goldner, A., Green, J., Müller, R., Markwick, P., Huber, M., 2014. A suite of early eocene (∼55 Ma) climate model boundary conditions. Geosci. Model. Dev. 7 (5), 2077–2090.
Hersbach, H., Bell, B., Berrisford, P., Hirahara, S., Horányi, A., Muñoz-Sabater, J., Nicolas, J., Peubey, C., Radu, R., Schepers, D., 2020. The ERA5 global reanalysis. Q. J. R. Meteorol. Soc. 146 (730), 1999–2049.
Hewitt, H.T., Bell, M.J., Chassignet, E.P., Czaja, A., Ferreira, D., Griffies, S.M., Hyder, P., McClean, J.L., New, A.L., Roberts, M.J., 2017. Will high-resolution global ocean models benefit coupled predictions on short-range to climate timescales? Ocean. Model. 120, 120–136.
Hirschi, J., Baehr, J., Marotzke, J., Stark, J., Cunningham, S., Beismann, J.-O., 2003. A monitoring design for the atlantic meridional overturning circulation. Geophys. Res. Lett. 30 (7), 1413.
Holmström, M., 2014. Eocene-oligocene benthic foraminifera stable isotope stratigraphy and paleoceanography of ODP site 757 and 756, ninetyeast ridge, southern Indian ocean.
Holton, L., Deshayes, J., Backeberg, B., Loveday, B., Hermes, J., Reason, C., 2017. Spatio-temporal characteristics of agulhas leakage: a model inter-comparison study. Clim. Dyn. 48, 2107–2121.
Hou, S., Stap, L.B., Paul, R., Nelissen, M., Hoem, F.S., Ziegler, M., Sluijs, A., Sangiorgi, F., Bijl, P.K., 2023. Reconciling southern ocean fronts equatorward migration with minor antarctic ice volume change during miocene cooling. Nat. Commun. 14 (1), 7230.
Huber, M., Brinkhuis, H., Stickley, C.E., Döös, K., Sluijs, A., Warnaar, J., Schellenberg, S.A., Williams, G.L., 2004. Eocene circulation of the southern ocean: Was antarctica kept warm by subtropical waters? Paleoceanography 19 (4).
Huber, M., Caballero, R., 2011. The early eocene equable climate problem revisited. Clim. Past 7 (2), 603–633.
Huck, C.E., van de Flierdt, T., Bohaty, S.M., Hammond, S.J., 2017. Antarctic climate, southern ocean circulation patterns, and deep water formation during the eocene. Paleoceanography 32 (7), 674–691.
Hughes, C.W., 2000. A theoretical reason to expect inviscid western boundary currents in realistic oceans. Ocean. Model. 2 (1–2), 73–83.
Hutchinson, K., Beal, L.M., Penven, P., Ansorge, I., Hermes, J., 2018. Seasonal phasing of agulhas current transport tied to a baroclinic adjustment of near-field winds. J. Geophys. Res.: Ocean. 123 (10), 7067–7083.
Ivany, L.C., Brey, T., Huber, M., Buick, D.P., Schöne, B.R., 2011. El Niño in the eocene greenhouse recorded by fossil bivalves and wood from antarctica. Geophys. Res. Lett. 38 (16).
Kennedy-Asser, A.T., Lunt, D.J., Valdes, P.J., Ladant, J.-B., Frieling, J., Lauretano, V., 2020. Changes in the high-latitude southern hemisphere through the Eocene–Oligocene transition: a model–data comparison. Clim. the Past 16 (2), 555–573.
Kirtland Turner, S., Ridgwell, A., Keller, A.L., Vahlenkamp, M., Aleksinski, A.K., Sexton, P.F., Penman, D.E., Hull, P.M., Norris, R.D., 2024. Sensitivity of ocean circulation to warming during the early eocene greenhouse. Proc. Natl. Acad. Sci. 121 (24), e2311980121.
Lambert, E., Le Bars, D., de Ruijter, W.P., 2016. The connection of the Indonesian throughflow, south Indian ocean countercurrent and the Leeuwin current. Ocean. Sci. 12 (3), 771–780.
Lamy, F., Winckler, G., Arz, H.W., Farmer, J.R., Gottschalk, J., Lembke-Jene, L., Middleton, J.L., Van der Does, M., Tiedemann, R., Alvarez Zarikian, C., et al., 2024. Five million years of antarctic circumpolar current strength variability. Nature 627 (8005), 789–796.

Le Hir, T., Penven, P., Huck, T., Pellen, R., Moulin, M., Rabineau, M., Aslanian, D., 2024. Impacts of the closure of the mozambique channel on the southwest Indian ocean circulation: A regional numerical simulation. J. Mar. Syst. 104024.

Lellouche, J.-M., Greiner, E., Le Galloudec, O., Garric, G., Regnier, C., Drevillon, M., Benkiran, M., Testut, C.-E., Bourdalle-Badie, R., Gasparin, F., 2018. Recent updates to the copernicus marine service global ocean monitoring and forecasting real-time 1/12° high-resolution system. Ocean Sci. 14, 1093–1126.

Li, D., Jing, Z., Cai, W., Zhang, Z., Shi, J., Ma, X., Gan, B., Yang, H., Chen, Z., Wu, L., 2024. Mesoscale eddies inhibit intensification of the subantarctic front under global warming. Environ. Res. Lett. 19 (11), 114054.

Lotfy, H., Heleika, M.A., Mostafa, R., Wahbah, D., 2017. Africa was still far south in the late ypresian: Paleomagnetic study on the early eocene 'minia'formation in central Egypt. NRIAG J. Astron. Geophys. 6 (2), 336–348.

Lunt, D.J., Bragg, F., Chan, W.-L., Hutchinson, D.K., Ladant, J.-B., Niezgodzki, I., Steinig, S., Zhang, Z., Zhu, J., Abe-Ouchi, A., et al., 2020. DeepMIP: Model intercomparison of early eocene climatic optimum (EECO) large-scale climate features and comparison with proxy data. Clim. Past Discuss. 2020, 1–27.

Lunt, D.J., Dunkley Jones, T., Heinemann, M., Huber, M., LeGrande, A., Winguth, A., Loptson, C., Marotzke, J., Roberts, C., Tindall, J., et al., 2012. A model–data comparison for a multi-model ensemble of early eocene atmosphere–ocean simulations: EoMIP. Clim. Past 8 (5), 1717–1736.

Lutjeharms, J.R.E., 2006. The Agulhas Current. Springer-Verlag.

Lutjeharms, J.R.E., Ansorge, I.J., 2001. The agulhas return current. J. Mar. Syst. 30 (1–2), 115–138.

Lutjeharms, J., Penven, P., Roy, C., 2003. Modelling the shear edge eddies of the southern agulhas current. Cont. Shelf Res. 23 (11–13), 1099–1115.

Marshall, G.J., 2003. Trends in the southern annular mode from observations and reanalyses. J. Clim. 16 (24), 4134–4143.

Martínez-Méndez, G., Zahn, R., Hall, I.R., Peeters, F.J., Pena, L.D., Cacho, I., Negre, C., 2010. Contrasting multiproxy reconstructions of surface ocean hydrography in the agulhas corridor and implications for the agulhas leakage during the last 345,000 years. Paleoceanography 25 (4).

Masters, J.C., Genin, F., Zhang, Y., Pellen, R., Huck, T., Mazza, P.P., Rabineau, M., Doucoure, M., Aslanian, D., 2021. Biogeographic mechanisms involved in the colonization of madagascar by african vertebrates: Rifting, rafting and runways. J. Biogeogr. 48 (3), 492–510.

McClelland, H.-L.O., Halevy, I., Wolf-Gladrow, D., Evans, D., Bradley, A.S., 2021. Statistical uncertainty in paleoclimate proxy reconstructions. Geophys. Res. Lett. 48 (15), e2021GL092773.

McDougall, T., Feistel, R., Millero, F.J., Jackett, D., Wright, D., King, B., Marion, G., Chen, C.-T.A., Spitzer, P., Seitz, S., 2009. The international thermodynamic equation of seawater 2010 (TEOS-10): Calculation and use of thermodynamic properties. Glob. Ship-Based Repeat Hydrogr. Man. IOCCP Rep. No 14.

McKinley, C.C., Thomas, D.J., LeVay, L.J., Rolewicz, Z., 2019. Nd isotopic structure of the Pacific ocean 40–10 Ma, and evidence for the reorganization of deep north Pacific ocean circulation between 36 and 25 Ma. Earth Planet. Sci. Lett. 521, 139–149.

Miller, K., Schmelz, W., Browning, J., Rosenthal, Y., Hess, A., Kopp, R., Wright, J., 2024. Global mean and relative sea-level changes over the past 66 Myr: implications for early eocene ice sheets. Earth Sci. Syst. Soc. 4 (1), 10091.

Njouodo, I.N., AS, M.R., Keenlyside, N., Koseki, S., 2021. Impact of the agulhas current on southern Africa precipitation: A modelling study. J. Clim. 1–50.

Peeters, F.J., Acheson, R., Brummer, G.-J.A., De Ruijter, W.P., Schneider, R.R., Ganssen, G.M., Ufkes, E., Kroon, D., 2004. Vigorous exchange between the Indian and atlantic oceans at the end of the past five glacial periods. Nature 430 (7000), 661–665.

Penven, P., Tedesco, P., Gula, J., Ménesguen, C., 2021. Mean barotropic vorticity balance in the south western Indian ocean. In: Proc. Nansen Tutu Center 10th Anniversary Symp.: Ocean, Weather and Climate, Science To the Service of Society, Cape Town, South Africa, Nansen Tutu Centre for Marine Environment Research. pp. 65–68.

Perren, B.B., Hodgson, D.A., Roberts, S.J., Sime, L., Van Nieuwenhuyze, W., Verleyen, E., Vyverman, W., 2020. Southward migration of the southern hemisphere westerly winds corresponds with warming climate over centennial timescales. Commun. Earth Environ. 1 (1), 58.

Rantanen, M., Karpechko, A.Y., Lipponen, A., Nordling, K., Hyvärinen, O., Ruosteenoja, K., Vihma, T., Laaksonen, A., 2022. The arctic has warmed nearly four times faster than the globe since 1979. Commun. Earth Environ. 3 (1), 168.

Reagan, J.R., Boyer, T.P., García, H.E., Locarnini, R.A., Baranova, O.K., Bouchard, C., Cross, S.L., Mishonov, A.V., Paver, C.R., Seidov, D., et al., 2024. World ocean atlas 2023. NOAA Natl. Centers Environ. Inf. Dataset: NCEI Access. 270533.

Reid, J.L., Brinton, E., Fleminger, A., Venrick, E.L., McGowan, J.A., 1978. Ocean circulation and marine life. In: Advances in Oceanography. Springer, pp. 65–130.

Richardson, P.L., 2007. Agulhas leakage into the atlantic estimated with subsurface floats and surface drifters. Deep Sea Res., Part I 54, 1361–1389.

Ridgway, K., Dunn, J., 2007. Observational evidence for a southern hemisphere oceanic supergyre. Geophys. Res. Lett. 34 (13).

Royer, D., Breecker, D., Polissar, P., Bowen, G., Henehan, M., Cui, Y., Steinthorsdottir, M., McElwain, J., Kohn, M., Pearson, A., et al., 2023. Toward a cenozoic history of atmospheric CO2. Science 382 (6675), eadi5177.

Rühs, S., Schmidt, C., Schubert, R., Schulzki, T.G., Schwarzkopf, F.U., Le Bars, D., Biastoch, A., 2022. Robust estimates for the decadal evolution of Agulhas leakage from the 1960s to the 2010s. Commun. Earth Environ. 3 (1), 318.

Saenko, O.A., 2006. Influence of global warming on baroclinic rossby radius in the ocean: A model intercomparison. J. Clim. 19 (7), 1354–1360.

Sætre, R., Da Silva, A.J., 1984. The circulation of the mozambique channel. Deep. Sea Res. Part A. Ocean. Res. Pap. 31 (5), 485–508.

Sallée, J.-B., Speer, K., Rintoul, S., Wijffels, S., 2010. Southern ocean thermocline ventilation. J. Phys. Oceanogr. 40 (3), 509–529.

Schmidt, C., Schwarzkopf, F.U., Rühs, S., Biastoch, A., 2021. Characteristics and robustness of Agulhas leakage estimates: an inter-comparison study of Lagrangian methods. Ocean. Sci. 17 (4), 1067–1080.

Schubert, R., Schwarzkopf, F.U., Baschek, B., Biastoch, A., 2019. Submesoscale impacts on mesoscale Agulhas dynamics. J. Adv. Model. Earth Syst. 11 (8), 2745–2767.

Schwarzkopf, F.U., Biastoch, A., Böning, C.W., Chanut, J., Durgadoo, J.V., Getzlaff, K., Harlaß, J., Rieck, J.K., Roth, C., Scheinert, M.M., Schubert, R., 2019. The INALT family – a set of high-resolution nests for the Agulhas current system within global NEMO ocean/sea-ice configurations. Geosci. Model. Dev. 12 (7), 3329–3355.

Sijp, W.P., England, M.H., 2008. The effect of a northward shift in the southern hemisphere westerlies on the global ocean. Prog. Oceanogr. 79 (1), 1–19.

Sluijs, A., Frieling, J., Inglis, G.N., Nierop, K.G., Peterse, F., Sangiorgi, F., Schouten, S., 2020. Late paleocene–early eocene arctic ocean sea surface temperatures: reassessing biomarker paleothermometry at Lomonosov Ridge. Clim. Past 16 (6), 2381–2400.

Soufflet, Y., Marchesiello, P., Lemarié, F., Jouanno, J., Capet, X., Debreu, L., Benshila, R., 2016. On effective resolution in ocean models. Ocean. Model. 98, 36–50.

Stammer, D., 1997. Global characteristics of ocean variability estimated from regional TOPEX/POSEIDON altimeter measurements. J. Phys. Oceanogr. 27, 1743–1769.

Steinig, S., Abe-Ouchi, A., de Boer, A.M., Chan, W.-L., Donnadieu, Y., Hutchinson, D.K., Knorr, G., Ladant, J.-B., Morozova, P., Niezgodzki, I., et al., 2024. Deepmip-eocene-p1: multi-model dataset and interactive web application for eocene climate research. Sci. Data 11 (1), 970.

Stewart, K.D., Haine, T.W., 2016. Thermobaricity in the transition zones between alpha and beta oceans. J. Phys. Oceanogr. 46 (6), 1805–1821.

Stokke, E.W., Jones, M.T., Tierney, J.E., Svensen, H.H., Whiteside, J.H., 2020. Temperature changes across the paleocene-eocene thermal maximum–a new high-resolution TEX86 temperature record from the eastern north sea basin. Earth Planet. Sci. Lett. 544, 116388.

Stramma, L., 1992. The south Indian ocean current. J. Phys. Oceanogr. 22 (4), 421–430.

Stramma, L., Lutjeharms, J.R., 1997. The flow field of the subtropical gyre of the south Indian ocean. J. Geophys. Res.: Ocean. 102 (C3), 5513–5530.

Su, L.-F., Zhang, Q.-Q., Sun, Y.-K., Zhang, S.-L., Smith, T., Li, C.-S., 2022. New evidence of the emergence of the east Asian monsoon in the early palaeogene. Sci. Rep. 12 (1), 20471.

Sverdrup, H.U., 1947. Wind-driven currents in a baroclinic ocean; with application to the equatorial current of eastern Pacific. Proc. Nat. Acad. Sci. U.S.A. 33, 318–326.

Tedesco, P., Gula, J., Penven, P., Ménesguen, C., 2022. Mesoscale eddy kinetic energy budgets and transfers between vertical modes in the Agulhas Current. Jpo 52, 677–704.

Theiss, J., 2004. Equatorward energy cascade, critical latitude, and the predominance of cyclonic vortices in geostrophic turbulence. J. Phys. Oceanogr. 34 (7), 1663–1678.

Tilburg, C.E., Hurlburt, H.E., O'Brien, J.J., Shriver, J.F., 2001. The dynamics of the east Australian current system: the tasman front, the east auckland current, and the east cape current. J. Phys. Oceanogr. 31 (10), 2917–2943.

Tim, N., Zorita, E., Emeis, K.-C., Schwarzkopf, F.U., Biastoch, A., Hünicke, B., 2019. Analysis of the position and strength of westerlies and trades with implications for agulhas leakage and south benguela upwelling. Earth Syst. Dyn. 10 (4), 847–858.

Tomczak, M., Godfrey, J.S., 1994. Regional Oceanography: An Introduction, first ed. Pergamon.

Toumoulin, A., Donnadieu, Y., Ladant, J.-B., Batenburg, S., Poblete, F., Dupont-Nivet, G., 2020. Quantifying the effect of the drake passage opening on the eocene ocean. Paleoceanogr. Paleoclimatology 35 (8), e2020PA003889.

Verma, D., Govil, P., Kumar, B., Khan, H., 2023. Variation in dynamics, controls, and impacts of agulhas leakage through late Pleistocene: A review. J. Palaeosciences 72 (1), 43–54.

Villa, G., Fioroni, C., Persico, D., Roberts, A.P., Florindo, F., 2014. Middle eocene to late oligocene antarctic glaciation/deglaciation and southern ocean productivity. Paleoceanography 29 (3), 223–237.

Wells, N., 2003. OCEAN CIRCULATION | general processes. In: Holton, J.R. (Ed.), Encyclopedia of Atmospheric Sciences. Academic Press, Oxford, ISBN: 978-0-12-227090-1, pp. 1528–1540.

West, C.K., Greenwood, D.R., Reichgelt, T., Lowe, A.J., Vachon, J.M., Basinger, J.F., 2020. Paleobotanical proxies for early eocene climates and ecosystems in northern north America from middle to high latitudes. Clim. Past 16 (4), 1387–1410.

Willard, D.A., Donders, T.H., Reichgelt, T., Greenwood, D.R., Sangiorgi, F., Peterse, F., Nierop, K.G., Frieling, J., Schouten, S., Sluijs, A., 2019. Arctic vegetation, temperature, and hydrology during early eocene transient global warming events. Glob. Planet. Change 178, 139–152.

Williams, C.J., Lunt, D.J., Salzmann, U., Reichgelt, T., Inglis, G.N., Greenwood, D.R., Chan, W.-L., Abe-Ouchi, A., Donnadieu, Y., Hutchinson, D.K., et al., 2022. African hydroclimate during the early eocene from the DeepMIP simulations. Paleoceanogr. Paleoclimatology 37 (5), e2022PA004419.

Yang, S., Matthias, K.G., 2007. The Optimal Relaxation Parameter for the SOR Method Applied to a Classical Model Problem. Technical Report, Technical Report TR2007–6, University of Maryland, Baltimore County.

Zhang, Y., de Boer, A.M., Lunt, D.J., Hutchinson, D.K., Ross, P., van de Flierdt, T., Sexton, P., Coxall, H.K., Steinig, S., Ladant, J.-b., 2022. Early eocene ocean meridional overturning circulation: The roles of atmospheric forcing and strait geometry. Paleoceanogr. Paleoclimatology 37 (3), e2021PA004329.

Zhang, Y., de Boer, A.M., Qin, G., Lunt, D.J., Hutchinson, D.K., Steinig, S., Niezgodzki, I., Wade, B.S., Liu, X., Poulsen, C.J., et al., 2025. Poleward expansion of north Pacific gyre circulation during the warm early eocene inferred from inter-model comparisons. Palaeogeogr. Palaeoclimatol. Palaeoecol. 661, 112712.

Zhang, Y., Huck, T., Lique, C., Donnadieu, Y., Ladant, J.-B., Rabineau, M., Aslanian, D., 2020. Early eocene vigorous ocean overturning and its contribution to a warm southern ocean. Clim. Past 16, 1263–1283.